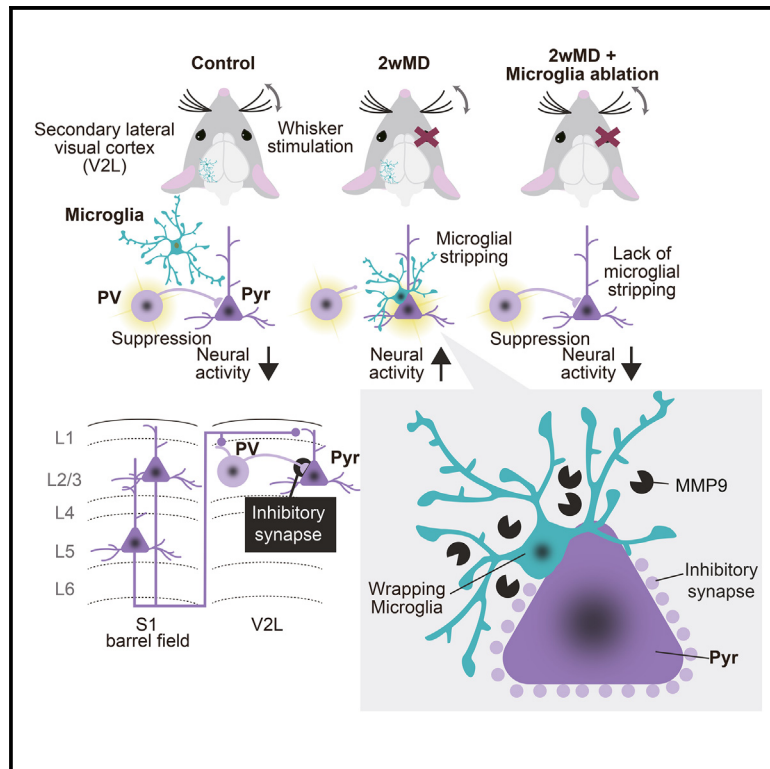# Microglia enable cross-modal plasticity by removing inhibitory synapses

Graphical abstract

Authors

Akari Hashimoto, Nanami Kawamura, Etsuko Tarusawa, ..., Andrew J. Moorhouse, Takeshi Yagi, Hiroaki Wake

Correspondence

hirowake@med.nagoya-u.ac.jp

In brief

Hashimoto et al. demonstrate that microglia are required for cross-modal plasticity after monocular deprivation. Through metalloprotease-dependent phagocytosis of inhibitory inputs, microglia enhance visual cortex excitability during whisker stimulation to enhance somatosensory discrimination ability. These results provide mechanisms for neural plasticity that can mediate behavioral adaptations following sensory loss.

Highlights

- Monocular deprivation in mice results in enhanced somatosensory discrimination

- Visual deprivation increases visual cortex (V2L) excitability during whisker stimulation

- Microglia phagocytose local inhibitory synapses to unmask cross-modal plasticity

- Matrix metalloproteinase 9 activity in V2L is required for cross-modal plasticity

CelPress

Article

Microglia enable cross-modal plasticity by removing inhibitory synapses

Akari Hashimoto,[1] Nanami Kawamura,[2] Etsuko Tarusawa,[2] Ikuko Takeda,[1] Yuki Aoyama,[1] Nobuhiko Ohno,[3,4] Mio Inoue,[1] Mai Kagamiuchi,[1] Daisuke Kato,[1] Mami Matsumoto,[5,6] Yoshihiro Hasegawa,[1] Junichi Nabekura,[7,13] Anne Schaefer,[8,9] Andrew J. Moorhouse,[10] Takeshi Yagi,[2] and Hiroaki Wake[1,11,12,13,14,15,*]

[1]Department of Anatomy and Molecular Cell Biology, Nagoya University Graduate School of Medicine, Nagoya 466-8550, Japan
[2]KOKORO-Biology Group, Laboratories for Integrated Biology, Graduate School of Frontier Biosciences, Osaka University, Suita 565-0871, Japan
[3]Department of Anatomy, Division of Histology and Cell Biology, Jichi Medical University, Shimotsuke 329-0498, Japan
[4]Division of Ultrastructural Research, National Institute for Physiological Sciences, Okazaki 444-8585, Japan
[5]Section of Electron Microscopy, Supportive Center for Brain Research, National Institute for Physiological Sciences, Okazaki 444-8585, Japan
[6]Department of Developmental and Regenerative Neurobiology, Institute of Brain Science, Nagoya City University Graduate School of Medical Sciences, Nagoya 467-8601, Japan
[7]Division of Homeostatic Development, National Institute for Physiological Sciences, Okazaki 444-8585, Japan
[8]Center for Glial Biology, Department of Neuroscience and Psychiatry, Friedman Brain Institute, Icahn School of Medicine at Mount Sinai, New York, NY 10029-6574, USA
[9]Max Planck Institute for Biology of Ageing, 50931 Cologne, Germany
[10]School of Biomedical Sciences, The University of New South Wales, Sydney, NSW 2052, Australia
[11]Division of Multicellular Circuit Dynamics, National Institute for Physiological Sciences, Okazaki 444-8585, Japan
[12]Center for Optical Scattering Image Science, Kobe University, Kobe 657-8501, Japan
[13]Department of Physiological Sciences, Graduate University for Advanced Studies, SOKENDAI, Hayama 240-0193, Japan
[14]Core Research for Evolutional Science and Technology, Japan Science and Technology Agency, Saitama 332-0012, Japan
[15]Lead contact
*Correspondence: hirowake@med.nagoya-u.ac.jp
https://doi.org/10.1016/j.celrep.2023.112383

SUMMARY

Cross-modal plasticity is the repurposing of brain regions associated with deprived sensory inputs to improve the capacity of other sensory modalities. The functional mechanisms of cross-modal plasticity can indicate how the brain recovers from various forms of injury and how different sensory modalities are integrated. Here, we demonstrate that rewiring of the microglia-mediated local circuit synapse is crucial for cross-modal plasticity induced by visual deprivation (monocular deprivation [MD]). MD relieves the usual inhibition of functional connectivity between the somatosensory cortex and secondary lateral visual cortex (V2L). This results in enhanced excitatory responses in V2L neurons during whisker stimulation and a greater capacity for vibrissae sensory discrimination. The enhanced cross-modal response is mediated by selective removal of inhibitory synapse terminals on pyramidal neurons by the microglia in the V2L via matrix metalloproteinase 9 signaling. Our results provide insights into how cortical circuits integrate different inputs to functionally compensate for neuronal damage.

INTRODUCTION

A striking manifestation of neural plasticity is adaptation that results from the loss of sensory input. The wiring of neural inputs from sensory receptors to their corresponding primary cortical regions requires the activity of these sensory pathways. When the sensory inputs are lost, the corresponding cortical regions can be wired to respond to other inputs. This was elegantly demonstrated in the developing visual system, where input from each eye could compete for the dominant visual cortex representation.[1] Similarly in somatosensory cortex, the representation of adjacent body regions is plastic. When a digit is

amputated, the cortical regions that previously responded to stimulation of the lost digit begin to respond to stimulation of adjacent digits.[2] Remarkably, this plasticity can extend across different sensory modalities. For example, humans who are blind from birth show greater abilities than sighted individuals in tactile discrimination, auditory localization, and pitch discrimination.[3–6] The occipital cortex of such blind individuals is activated by somatosensory or auditory stimuli, and this cross-modal cortical plasticity is associated with enhanced functional abilities.[7–9] Cross-modal plasticity following the loss of vision, hearing, or vibrissa sensation has also been demonstrated in mice. This has enabled further investigation of the underlying neural

mechanisms.[10–13] Since certain aspects of cross-modal plasticity can manifest within hours of sensory deprivation,[14] it has been suggested that they arise from the strengthening of existing neural pathways. This can either occur through axonal projections directly connecting different cortical regions or via divergence of thalamic or other subcortical relay afferents. There is a dearth of information on the mechanisms by which these neural pathways are strengthened after sensory loss and their relationship to enhanced behavior. Homosynaptic strengthening of excitatory connections (e.g., via long-term potentiation), branching of excitatory afferents, and altered excitatory/inhibitory balance may contribute to cross-modal plasticity.[11,15] Elucidating these cellular mechanisms may help to enhance compensation in individuals deprived of a peripheral sensory organ. It may also help functional recovery following stroke, where similar plasticity mechanisms are likely to apply.[16,17] Furthermore, the mechanisms of cross-modal plasticity provide broader insights into how different sensory modalities are integrated by the brain in healthy and disease states.[13,18] Therefore, in the present study we induced monocular deprivation (MD) in developing mice and studied the resultant compensatory adaptations in somatosensory responses using a combination of *in vivo* imaging, electrophysiology, biochemical measurements, molecular manipulation, and behavioral assays. We demonstrate the cross-modal plasticity of neural circuits within the secondary visual cortex associated with enhanced vibrissae touch discrimination. As microglia sculpt neuronal circuits during development and modification following sensory deprivation,[19–21] we hypothesized that microglia contribute to this cross-modal plasticity and probed the underlying mechanisms. Our results indicate that microglia selectively phagocytose inhibitory inputs to visual cortical neurons to enable greater response levels during somatosensory stimulation. Matrix metalloproteinase 9 (MMP9) plays a key role in this plasticity. Blocking MMP9 or transient ablation of microglia prevented both the circuit rearrangements and the enhanced somatosensory discrimination following MD. Taken together, we further reveal the cellular and molecular sequences of microglia-dependent events that are sufficient to mediate cross-modal plasticity and behavioral compensation following visual deprivation.
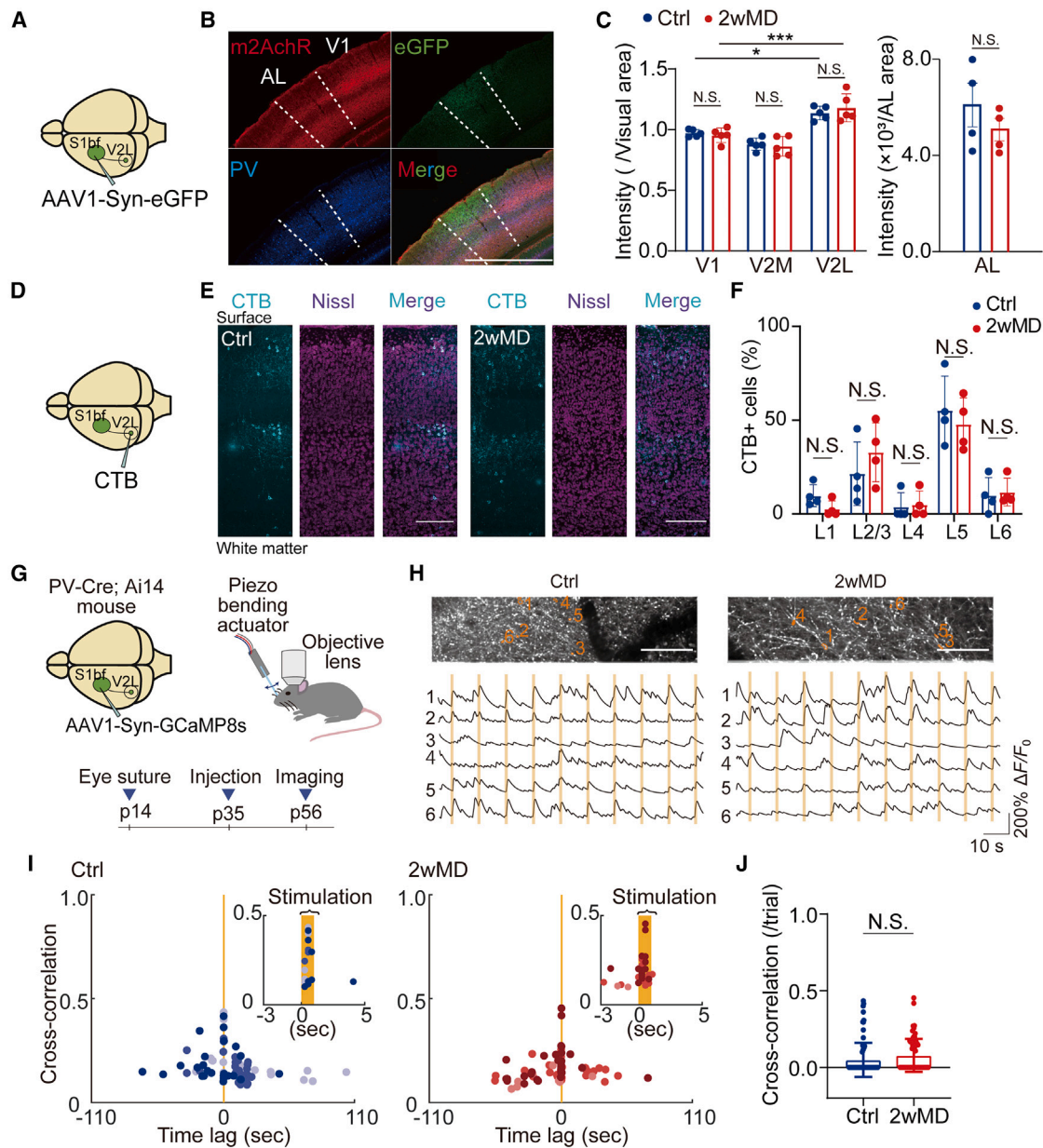
RESULTS

Whisker stimulation activates S1-V2L connections
Corticocortical projections have been demonstrated between different sensory cortical areas.[22] We first probed for functional connections between the somatosensory and visual cortices and possible changes after MD. Primary somatosensory cortex barrel field (S1bf) neurons were labeled through local administration of enhanced green fluorescent protein (eGFP)-coded adeno-associated virus (AAV). Subsequently, their axonal projections to visual-associated cortical areas were examined (Figure 1A). The eGFP-labeled S1bf axons were observed across the primary (V1) and secondary (V2) cortices, with their highest density in the lateral V2 region (V2L, extrastriate visual area) (Figures 1B and 1C). The induction of MD through eyelid suturing on postnatal day 14 (2wMD) did not alter the intensity of S1 projections (Figure 1C). Within the V2L subcortical area, we

observed staining in an anterolateral area (AL), which was characterized by a lower density of parvalbumin (PV) neurons and low expression levels of muscarinic type 2 acetylcholine receptors (m2AchR), reflecting a region of high axonal density (Figures 1B and S1A). The 2wMD group did not alter the intensity of the S1bf projections in the AL (Figures 1B and 1C). The number of AAV-labeled neurons in the S1bf did not differ between the control and 2wMD mice (Figure S1B). To label these S1-V2L projections, we injected cholera toxin B subunits bound to Alexa 488 into layers 2/3 of the V2L (Figure 1D). Since cholera toxin is taken up into nerve terminals before their retrograde transportation to the soma, subsequent visualization of immunofluorescence-positive neurons in the S1bf confirmed that these S1bf axons terminated in the V2L (Figures 1E and 1F). Furthermore, retrograde labeling using AAV combined with immunohistochemistry suggested that the S1bf populations projecting to the AL were mostly distributed in the septal regions of the barrel cortex (Figure S1C). We examined the functional activity of these S1bf-V2L projections by injecting an AAV-coded synaptic-protein-tagged Ca^{2+} indicator into S1bf (Syn-GCaMP8s[23]) (Figure 1G) and conducted *in vivo* imaging of the terminal axons and boutons in layer 1 of the V2L (Figure 1H). The synaptic terminal regions in less-dense PV^+ neuron areas were identified by crossing PV-Cre mice with Ai14 mice.[24] The Ca^{2+} transients were phase-locked to whisker deflections (Figure 1I). These stimulation-induced S1-V2L axonal responses were similar between control and 2wMD mice (Figures 1I and 1J). Together, these results indicate that cross-cortical projections between S1bf and V2L are present in our mouse model and are activated by whisker stimulation. However, the density or activity of these cross-cortical projections is not affected by visual deprivation.

MD mice show higher V2L activity during complex tactile stimulation
Subsequently, we examined whether whisker-evoked responses could be measured in V2L neurons. Using AAV-mediated GCaMP6f expression, we imaged the Ca^{2+} activity in V2L L2/3 neurons. Initially, we used a simple stimulus that mechanically deflected all whiskers back and forth simultaneously (Figures S1D–S1F). The Ca^{2+} transients in V2L neurons were largely spontaneous, with only a small proportion of responses (<16% of neurons) phase-locked to mechanical deflections. Furthermore, the incidence and synchrony of these neuronal responses were not affected by 2wMD (Figures S1G–S1I). We also examined V2L neuronal responses to more complex patterns of whisker stimulation by rubbing rough- or smooth-textured sandpaper (see STAR Methods) (Figures 2A and 2B). In control mice, the total frequency of Ca^{2+} transients during rough sandpaper stimulation decreased (Figures 2C, 2D, S1J, and S1K), thereby suggesting an inhibition of V2L neuronal activity during whisker stimulation. In 2wMD mice, there was a proportion of neurons whose Ca^{2+} activity was actually higher during sandpaper stimulation (Figures 2C, 2D, and S1K). When V2L neurons were stratified based on their average spontaneous firing rates (black vertical lines, Figures 2C and 2D) to select neurons with above-average activity, the absolute frequency of Ca^{2+} transients during whisker stimulation was significantly greater in 2wMD mice than that in control mice (Figure 2E). On the contrary, the

Figure 1. Cross-sensory S1bf-V2 projections are functional but unchanged by monocular deprivation at P14 (2wMD)

(A and B) Green fluorescent protein (GFP)-labeled S1bf axonal projections to the visual cortices and particularly to the subcortical AL area in V2L. Scale bar, 1 mm.

(C) Relative fluorescence intensity of GFP in visual cortical areas between 2wMD and control mice, with the V2L showing the greatest intensity.

(D) Experimental scheme for the retrograde labeling of V2L neurons.

(E) Typical images of retrogradely labeled neurons in the S1bf, from surface (upper) through to layer 6 (lower), for control and 2wMD mice. Magenta: Nissl staining; cyan: CTB-Alexa 488 staining. Scale bars, 200 μm.

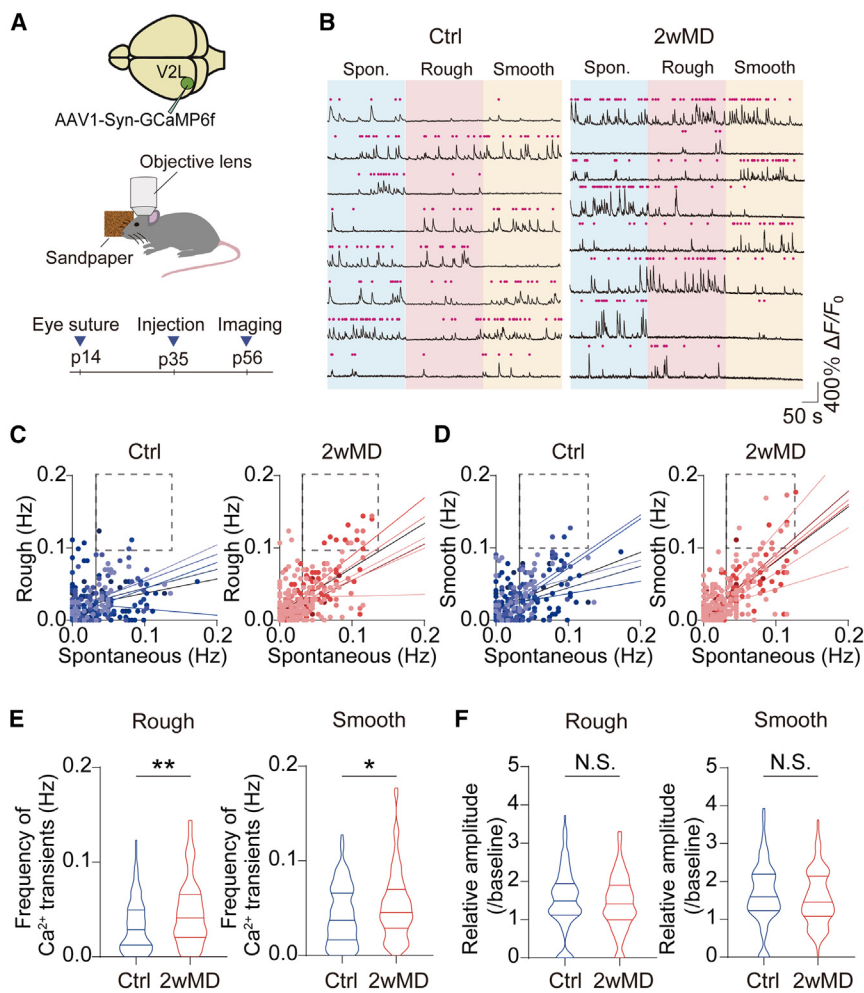(F) Quantification of the density of CTB-labeled cells.

(G) Ca^{2+} transients in S1bf axonal projections were imaged in the L1 of V2L under whisker stimulation with back-and-forth movements of a swinging plate.

(H) Representative Ca^{2+} fluorescence of eight different terminal axon segments (as numbered; left panels), and the timing of the examined Ca^{2+} transients relative to whisker deflections, indicated by vertical orange lines (right panels). Scale bars, 50 μm.

(I) Temporal correlation of Ca^{2+} transients with whisker stimuli in 2wMD and control mice. The upper right inset column graph expands the period during whisker stimulation.

(J) There was no difference in the mean proportion of boutons responding to each whisker stimuli between the control and 2wMD mice.

Data shown as mean ± SD. N.S., not significant.

Figure 2. V2L neurons show increased excitability during whisker stimulation following monocular deprivation

(A) Simplified experimental scheme.

(B) Typical traces of Ca^{2+} transients in single V2L neurons from control (Ctrl) or 2wMD mice, during basal periods (Spon), and during periods when rough or smooth sandpaper are presented to whiskers. Individual Ca^{2+} transients are indicated by red dots above each trace.

(C and D) Correlations between the spontaneous and whisker-related frequency of Ca^{2+} transients during rough (C) or smooth (D) sandpaper stimulation. Data obtained from each mouse are fit using a regression line, with the mean regression shown in black. Vertical bar delineates the averaged spontaneous firing frequency during basal periods.

(E) Absolute mean frequency of Ca^{2+} transients during whisker stimulation. The plots show all events from neurons with above-average basal activity rates.

(F) The amplitudes of Ca^{2+} transients (expressed relative to the mean amplitude during basal conditions) were similar in control and 2wMD mice.

amplitude of Ca^{2+} transients was unaffected by 2wMD (Figure 2F). Furthermore, the proportion of the V2L neuronal population that responded to rough sandpaper with an increase in the frequency of Ca^{2+} transients was significantly higher in 2wMD mice than in control mice (Figure S1L). We conclude that MD induces cross-modal activation of V2L.
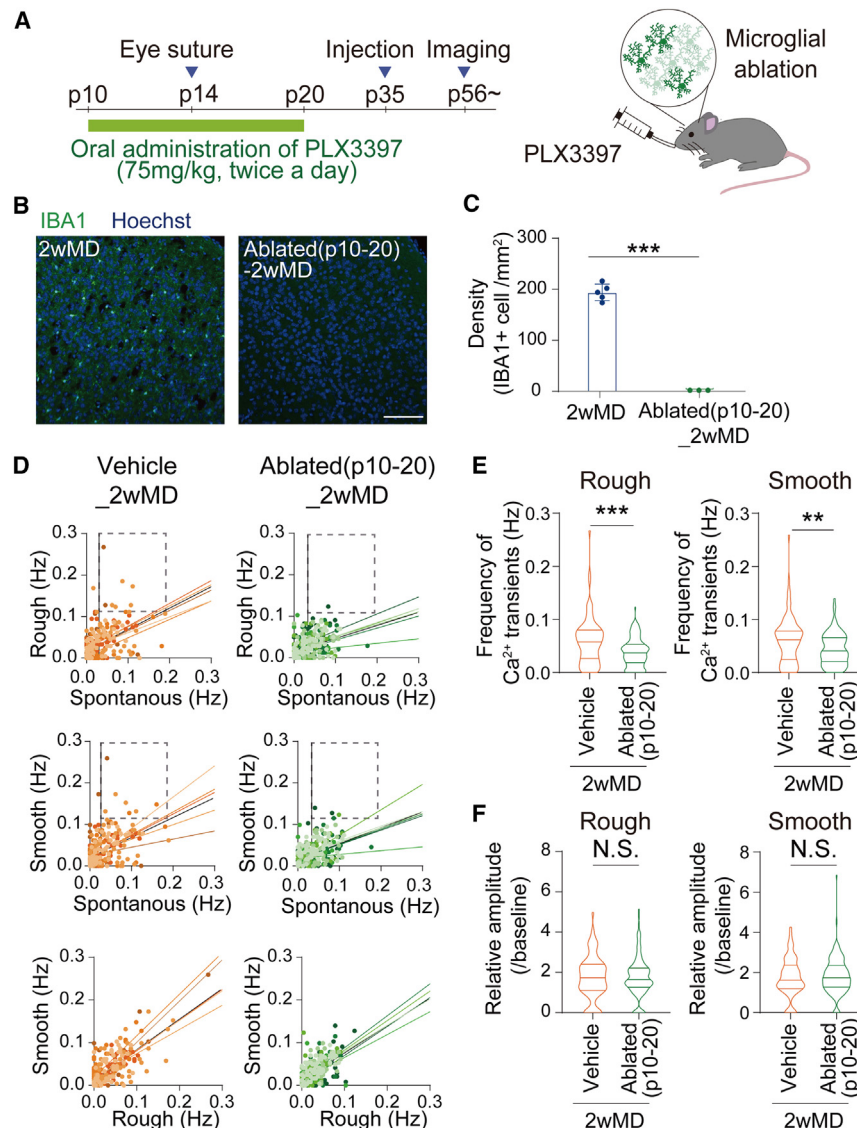
Characterization of the time course of enhanced V2L activity in MD mice

Next, we examined whether the cross-modal enhanced activation of V2L occurred largely within the critical period of the visual system (~postnatal day 40 [p40]) or developed uniformly over time after MD. We performed Ca^{2+} imaging of 2wMD mice at p21 and p41 and compared the results with p56 data (Figure S2A). To assess the extent of cross-modal V2L activation, we subtracted the spontaneous frequency of Ca^{2+} transients from that during rough or smooth sandpaper representation (ΔFrequency). At p21, 2wMD showed a significant increase in ΔFrequency for both rough and smooth sandpaper when compared with control mice, and this was also seen at p41 (Figure S2B). At p56, ΔFrequency was significantly increased for rough sandpaper stimulation (Figure S2B). Across all ages,

control mice showed a negative mean ΔFrequency (Figures S2B and S1J). This suggested that cross-modal plasticity occurred within this critical period. We also observed cross-modal enhanced V2L activity after binocular deprivation at p14 (2wBD, imaged at p56), which was significantly greater than what was observed after 2wMD (Figure S2C). Finally, we examined whether MD near the end of the critical period (p35, 5wMD) induced cross-modal V2L activation (Figures S2D–S2G). A significant increase in the frequency of Ca^{2+} transients during sandpaper stimulation was again observed. However, this was counterbalanced by a decrease in the amplitude of Ca^{2+} transients (Figures S2E–S2G).

Cross-modal activation of subpopulations of V2L inhibitory neurons in MD mice

Next, we examined whether MD-induced cross-modal activation extended to V2L inhibitory neurons by imaging Ca^{2+} transients in both parvalbumin-positive (PV^+) and somatostatin-positive (SST^+) L2/3 neurons in response to sandpaper stimulation (Figures S3 and S4). The PV^+ neurons showed a pattern similar to that of pyramidal neurons when we used simple mechanical deflection. No major changes in Ca^{2+} transients were observed in either the control or 2wMD mice (Figures S3A–S3F). Upon extraction of the above-average neuronal population, we observed an increase in the frequency of Ca^{2+} transients in 2wMD mice during sandpaper stimulation (Figures S3G–S3L). In contrast, 2wMD did not induce any detectable changes in the frequency of Ca^{2+} transients in SST^+ neurons during sandpaper stimulation (Figures S4A–S4D). The relative amplitudes of Ca^{2+} transients did not differ between control and 2wMD

A

Eye suture   Injection   Imaging

p10   p14   p20   p35   p56~

Oral administration of PLX3397
(75mg/kg, twice a day)

Microglial ablation

PLX3397

B IBA1 Hoechst

2wMD

Ablated(p10-20)
-2wMD

C

D Vehicle_2wMD   Ablated(p10-20)_2wMD

E Rough   Smooth

F Rough   N.S.   Smooth   N.S.

Figure 3. Pharmacological ablation of microglia prevents the increased excitability seen in 2wMD mice

(A) Experimental scheme for pharmacological microglia ablation.

(B and C) Sample immunohistology sections (B) and quantification (C) of the V2L microglia density at p20 in vehicle and PLX3397-treated 2wMD mice showing the loss of microglia (stained using IBA1, green) and co-localized nuclear stain (Hoechst, blue). Scale bar, 100 μm.
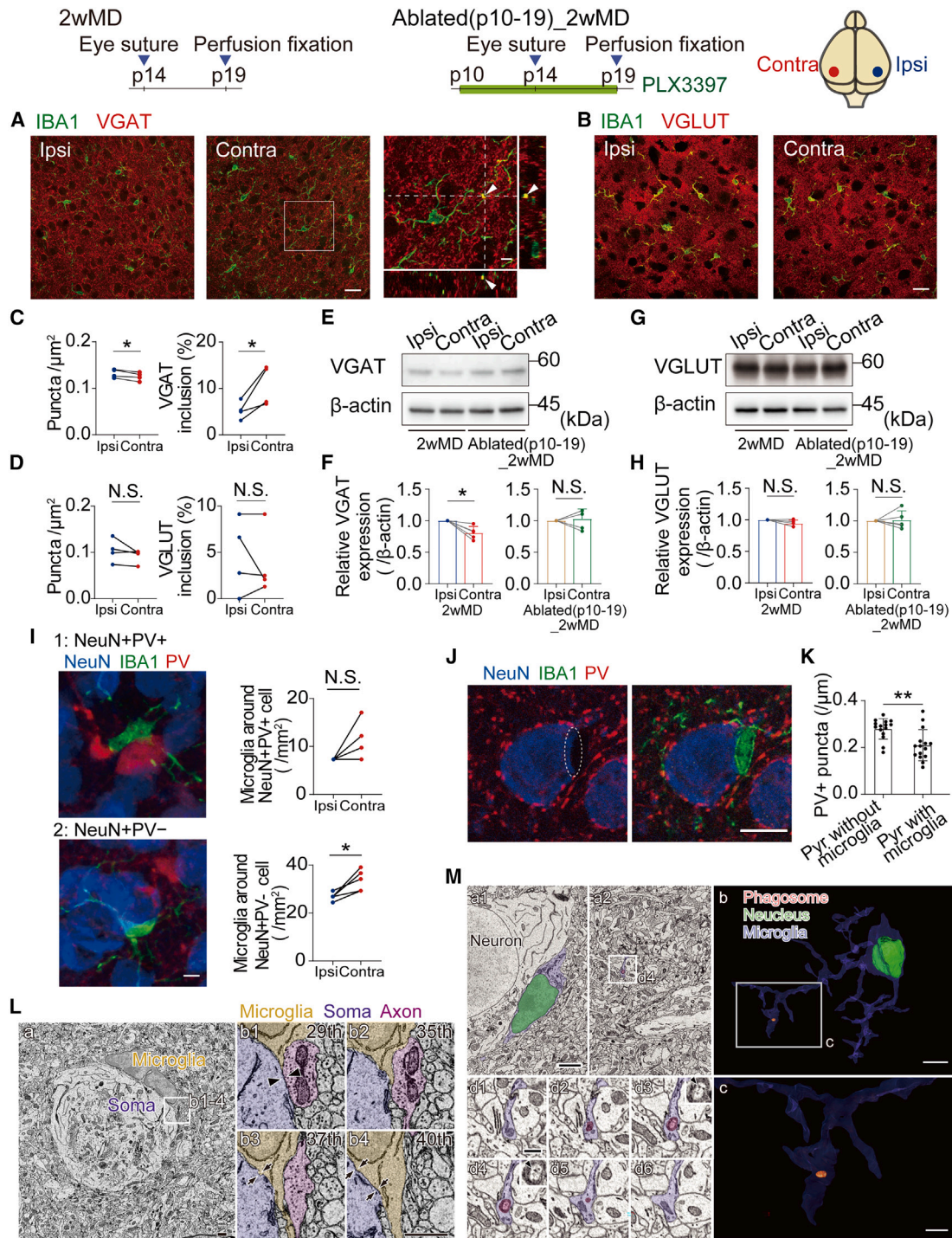
(D) Correlation between the frequency of Ca^{2+} transients during basal periods (spontaneous) and during periods of whisker stimulation (rough, upper graphs; or smooth sandpaper, middle graphs) in vehicle (left, vehicle_2wMD) and microglia-ablated (right, ablated_2wMD) mice both after 2wMD. Vertical bar delineates the averaged spontaneous firing frequency. Bottom graphs show the frequency of Ca^{2+} transients during whisker stimulation with rough sandpaper plotted against that during whisker stimulation with smooth sandpaper in vehicle_2wMD (left) or in ablated_2wMD (right) mice with the mean regression line shown in black.

(E and F) Microglia ablation significantly reduced the frequency of Ca^{2+} transients after 2wMD as compared with vehicle-treated mice (E) but did not affect the amplitude of Ca^{2+} transients (F).

Data shown as mean ± SD.

mice during whisker stimulation for any of the examined neuron population (Figures 2F, S3K, and S4D).

Microglia contribute to enhanced excitability after MD

The Ca^{2+} imaging results suggest altered excitability within the V2L, giving rise to larger responses during more complex somatosensory stimulation after MD. In line with our original hypothesis, we hypothesized as to whether this arose from altered neural circuit wiring involving microglia-mediated structural plasticity. Therefore, we used a pharmacological approach to deplete microglia[25] by daily administration of pexidartinib (PLX3397) from p10 to p20 (ablated[p10–20]_2wMD). The eyelids were sutured on day 14, and *in vivo* imaging of the V2L layers 2/3 was performed at 8 weeks (Figure 3A). The Ca^{2+} activity was compared against vehicle-injected mice (vehicle_2wMD). As expected, the PLX3397 dosing strategy almost completely depleted microglia (Figures 3B and 3C). Vehicle-

treated 2wMD mice showed a population of V2L neurons with increased responses during rough and smooth sandpaper stimulation. This was less evident in microglia-ablated mice (Figure 3D). When we analyzed neurons with an above-average frequency of basal Ca^{2+} transients, there was a significant decrease in activity during whisker stimulation in ablated(p10–20)_2wMD mice compared with vehicle_2wMD mice. However, the amplitude of Ca^{2+} transients was not affected by microglial ablation (Figures 3E and 3F). We propose that the loss of microglia when circuits were undergoing plasticity after 2wMD prevented the cross-modal enhancement of V2L activity. Maternal administration of PLX3397 between p1 and p10 to transiently ablate immature microglia prior to 2wMD (ablated[p1–10]_2wMD) had no significant effect on the V2L neuronal response to sandpaper stimulation (Figures S5A–S5C). However, microglial ablation after 2wMD, by treatment with PLX3397 from p35 to p45 (ablated[p35–45]_2wMD; Figure S5D), reduced cross-modal enhancement of V2L excitability (Figures S5D–S5F). This might be indicative that the ongoing microglial activity is required to sustain cross-modal plasticity. When microglia were ablated at a later developmental period, just after MD, now performed at p35 (ablated[p35–45]_5wMD), there was a significant decrease in cross-modal enhanced V2L excitability (Figures S5G–S5I). Finally, we ablated microglia following PLX3397 treatment from p10 to p20 in control mice (without

Figure 4. Molecular and histological evidence for microglial phagocytosis of GABAergic synapses onto excitatory V2L neurons following 2wMD

(A and B) Representative images showing co-staining of IBA1 and inhibitory (VGAT) or excitatory (VGlut) synapse markers in the contralateral and ipsilateral V2L of 2wMD mice. The right-hand panel in (A) shows a magnified image and its orthogonal views of the boxed contra region. Scale bar, 20 μm; scale bar in expanded image in (A), 5 μm. The arrowheads indicate VGAT puncta in microglia.

(C and D) quantification of the density (left panels) and proportion of puncta within IBA1 immunoreactivity (right panels) for VGAT (C) and VGlut (D).

(E and G) Representative western blots of VGAT (E) and VGlut (G) protein expression levels in the ipsilateral and contralateral V2L of 2wMD and microglia-ablated 2wMD mice.

(legend continued on next page)

MD) and examined the sandpaper-induced responses at p56 (Figure S5J). Interestingly, we observed significant decreases in both the frequency and amplitude of V2L neuron Ca^{2+} transients compared with vehicle-treated mice (Figures S5J–S5L), indicating that developmental microglia affect V2L excitability independently of MD.

Microglia "strip" inhibitory synapses after MD

Complement component 1q (C1Q) expression increases alongside microglial phagocytosis of synapses, thereby indicating its activity as a phagocytosis tag.[26] The relative levels of C1Q co-localized with ionized calcium-binding adapter molecule 1 (IBA1) in the contralateral V2L increased after 2wMD (Figure S6A). As a regional control, we observed no differences in the co-localization of C1Q with IBA1 in the S1 cortex of 2wMD mice (Figure S6A). This pattern of changes in V2L (increased *C1qa*, see also Figure 7A, C1Q) is consistent with increased microglia-mediated synapse phagocytosis. Therefore, we immune-stained for vesicular γ-aminobutyric acid (GABA) transporter (VGAT) and vesicular glutamate transporter (VGlut), which are protein markers of inhibitory and excitatory presynaptic terminals, respectively (Figures 4A–4D). Again, we compared the contralateral V2L in 2wMD mice with the ipsilateral controls. There was a decrease in the relative number of VGAT-positive puncta in the contralateral V2L and an increase in VGAT puncta inclusion in IBA1-identified microglia (Figures 4A and 4C). Consistently, the total VGAT protein decreased in the contralateral V2L, 5 days after 2wMD but not at 3 days after 2wMD (Figures 4E, 4F, and S6B). In contrast, there were no differences in VGlut puncta (and their inclusion in microglia) or total VGlut protein levels between the contralateral and ipsilateral V2L (Figures 4B, 4D, 4G, and 4H). Pharmacological ablation of microglia (as described above; ablated[p10-19]_2wMD) prevented these MD-induced changes in VGAT protein levels without affecting VGlut protein levels (Figures 4F and 4H). Together, this suggests a microglia-dependent, selective phagocytosis of inhibitory terminals after 2wMD. Also, we consistently observed an increased population of microglia surrounding the soma of excitatory neurons in the contralateral V2L area, although the number of PV^+ neurons did not change (Figures 4I and S6C;

Video S1). This is akin to the greater microglial "wrapping" of olfactory bulb neurons after occlusion of nares in another mouse sensory deprivation model.[27] Notably, there was evidence of fewer PV^+ puncta at these sites of microglia-neuron "wrapping" (Figures 4J and 4K; Video S1). Electron microscopy showed examples of microglia adjacent to pyramidal neurons interspersing their processes between inhibitory boutons and the plasma membrane of the soma, suggesting they are "stripping" inhibitory synapses (Figure 4L). Finally, some inhibitory terminal markers were observed inside the microglia (Figure 4M and Video S2).

A selective decrease in inhibitory connections after MD

The Ca^{2+} imaging studies detected microglia-dependent increases in V2L activity during whisker stimulation after MD. However, imaging is complicated by the nature of this broad population response. Only a subset of V2L neurons may be associated with somatosensory inputs, including spontaneously active neurons and the ones that are potentially responsive to bilateral visual inputs or other modalities that also contribute to the response profiles. To examine neural circuit changes more specifically, we utilized patch-clamp recordings in cortical brain slices from mice with prior injection of AAV-encoded channel rhodopsin (ChR2) into the S1bf. This would optically activate S1bf afferent inputs to the V2L. Furthermore, we utilized PV-tdTomato mice for these experiments. This would simultaneously patch onto both excitatory pyramidal (Pyr) and PV^+ inhibitory neurons (Figures 5A and 5B). First, we optically activated S1bf afferents to confirm that the patched Pyr and PV^+ neurons both responded to projections from the S1bf (Figure 5C, left panels). Most recorded Pyr and PV^+ neurons received synaptic inputs from these S1bf projections (Figure S7A) with a synaptic current latency clustered around 4 ms. Perfusion with tetrodotoxin (TTX) and 4-aminopyridine (4-AP) treatments, predicted to favor photoexcitation of direct inputs over polysynaptic inputs, did not shorten the excitatory postsynaptic current (EPSC) latency. Therefore, photostimulation evoked direct monosynaptic inputs in both Pyr and PV^+ V2L neurons (Figure S7B). Most Pyr-PV^+ neuron pairs also had reciprocal synaptic connections. Stimulation of a Pyr neuron evoked a unitary

---

(F and H) Quantification of the protein expression ratios in the contralateral V2L relative to the ipsilateral V2L, in 2wMD and 2wMD microglia-ablated mice, for VGAT (F) and VGlut (H).

(I) Co-staining of microglia (IBA1), neurons (NeuN), and inhibitory neurons (PV) in the V2L of 2wMD mice. Representative images showing microglia wrapping around an inhibitory PV (NeuN+, PV+) and excitatory neuron (NeuN+, PV−). Scale bar, 5 μm. The plots to the right quantify these associations.

(J) Magnified images from the contralateral V2L of a 2wMD mouse showing microglia (green) around an excitatory neuron (blue) to demonstrate the absence of inhibitory terminals (red) at the site of microglial contact. Scale bar, 10 μm. See also Video S1.
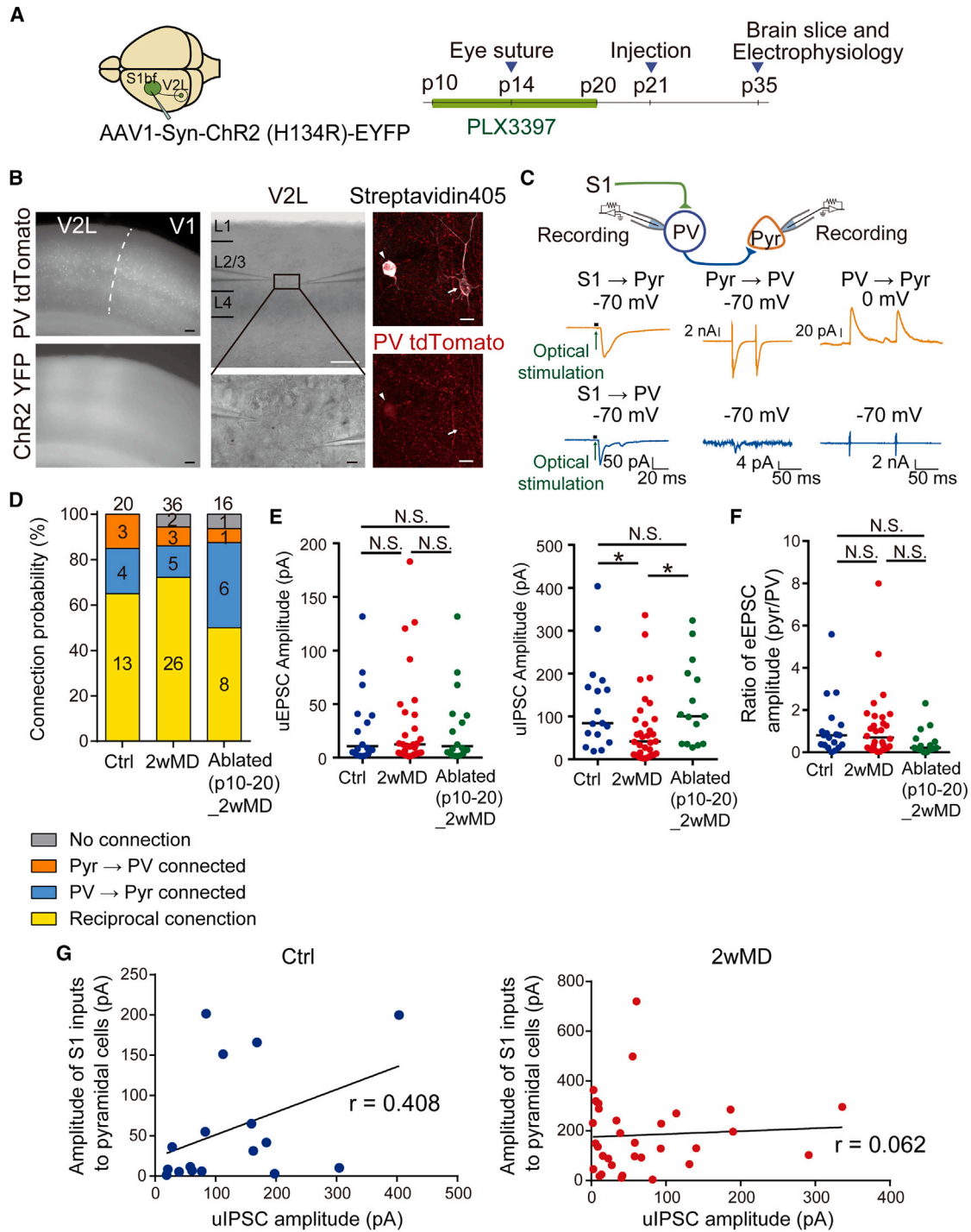
(K) There was a significant reduction in the number of these PV^+ puncta on excitatory neurons contacting microglia (Pyr with microglia), as compared with those not contacting microglia (Pyr without microglia).

(L) Representative electron microscopic images of the contralateral V2L of a 2wMD mouse. Panel (a) shows a lower-magnification image of a microglia associated with an excitatory neuron. The region of interaction outlined in the box of panel (a) is expanded in the right-hand panels (b1–b4), and the serial magnified images are on the right images (b1–b4), which show the serial section numbers and color code the microglia (yellow), neuronal soma (purple), and presynaptic axon (pink) with en-passant bouton. The arrowhead indicates the synaptic cleft that is characterized by vesicle containing axonal terminal, and the arrow indicates the contact site between microglia and neuronal cell soma. Scale bars, 10 μm for low-magnification image and 1 μm for high-magnification image.

(M) Phagocytosis of presynaptic elements by microglia in cross-modal plasticity. One of the serial electron microscopic images (a1, a2) and their three-dimensional (3D) reconstruction at low (b) and high (c) magnification show one of the microglial processes (blue) containing engulfed or phagocytosed presynaptic elements (red). The serial electron microscopic images at higher magnification (d) demonstrate phagosome with synaptic vesicles (arrowheads) in the microglial process (d insets, arrowheads). The marked areas (a, b) are magnified (c, d), and the phagosome is magnified in the insets (d3, d4). The nucleus of the microglia is labeled in the electron microscopic image and 3D reconstruction (green). Scale bars, 2 μm (a), 3 μm (b), 1 μm (c), and 500 nm (d).

Data shown as mean ± SD.

Figure 5. Monocular deprivation selectively reduces local inhibitory synaptic responses

(A) Experimental protocol for electrophysiological experiments.

(B) Double-patch-clamp recordings were performed in layer 2/3 of the V2L cortex in mouse brain slices, with PV^{+} neurons identified through tdTomato expression and with S1bf afferent inputs expressing ChR2-EYFP. Arrows and arrowheads in the right panel indicate recorded large PV[−] (Pyr neurons) and PV[+] (PV) neurons, respectively. Scale bars, 100 μm (black line) and 10 μm (white line).

(C) Synaptic input mapping in the V2L through paired recordings/stimulation of Pyr and PV^{+} neurons and selective ChR labeling of S1bf afferents (upper schematic). Lower panels show sample responses from Pyr neurons (middle panel) or PV^{+} neurons (lower panel) in response to optical stimulation of S1bf afferent responses (left), following Pyr stimulation (center), and after PV[+] neuron stimulation (right).

(D) Synaptic connectivity distribution in the PV[+] and pyramidal cells of control, 2wMD, and microglia-ablated mice.

(legend continued on next page)

EPSC (uEPSC) in a PV$^+$ neuron, and stimulation of a PV$^+$ neuron evoked a unitary inhibitory postsynaptic current (uIPSC) in the paired Pyr neuron (Figure 5D). The proportion of these reciprocal connections, the amplitude of the uEPSCs, and the ratio of S1bf-evoked Pyr/PV EPSC amplitudes were not changed by 2wMD (Figures 5C, 5E [left], and 5F). However, the amplitudes of uIPSCs evoked by PV stimulation were significantly decreased by 2wMD (Figure 5E, right). In addition, the number of uIPSC failures and uIPSC coefficient of variance (see STAR Methods) increased in 2wMD mice (Figures S7C and S7D). These results suggest a selective loss of inhibitory synaptic inputs to Pyr from local circuit PV$^+$ interneurons in 2wMD mice. In control mice, a larger S1bf evoked EPSC in Pyr neurons. This correlated with a larger uIPSC in those neurons. A similar, albeit weaker, correlation was observed between S1bf-evoked EPSCs in PV$^+$ neurons and IPSC amplitudes. However, this correlation was absent in 2wMD mice (Figures 5G and S7E), which is consistent with the loss of synaptic inhibition from PV$^+$ neurons within the S1 to V2L circuit. In 2wMD mice treated with PLX3397 to ablate microglia (as above; ablated[p10–20]_2wMD), the changes observed in inhibitory synaptic currents were prevented (Figures 5E, S7C, and S7D), indicating a similar dependence on microglia, as seen for V2L responses to tactile stimulation.

Cross-modal behavioral plasticity depends on microglia

Next, we investigated whether microglia-dependent changes in V2L inhibitory circuits and the increase in excitability during evoked whisker stimulation were sufficient to induce behavioral compensation. Mice were trained in a whisker-dependent texture discrimination task. Here, a water bolus rewarded the correct detection of smooth sandpaper presented to the whiskers, whereas an unpleasant air puff resulted from incorrect responses to rough sandpaper (Figures 6A–6C and S8A). Mice were first pre-trained to correctly detect smooth sandpaper (i.e., without punishment), and mice that reached a 70% success ratio in 2 days proceeded to the main discrimination task. The 2wMD mice performed significantly better than control mice during the first 2 days of pre-training and typically progressed quicker to the main task (Figures 6D, S8B, and S8C). In the main discrimination task, MD mice performed better than control mice, with a significantly larger increase in success ratios over time (Figure 6D). To confirm the involvement of V2L in this whisker discrimination task, we locally applied muscimol to the brain surface above the V2L in 2wMD mice (muscimol_2wMD) using the Elvax-elution delivery system. Enhanced performance during both the pre-training and discrimination tasks was absent in muscimol-treated mice (Figures 6A and 6D). In MD mice with microglial ablation using PLX3397 (ablated[p10–20]_2wMD), enhanced performance during pre-training and the discrimination task was again absent (Figures 6E, S8B, and S8C). Finally, MD (5wMD) did not induce enhanced sensory discrimination, suggesting that MD

within the critical period is required for robust cross-modal plasticity (Figures S8D–S8F).

MMP9 inhibition prevents cross-modal plasticity

Since pharmacological ablation of microglia prevented several aspects of cross-modal plasticity, we probed changes in gene expression in V2L microglia following 2wMD and 5wMD (Figures 7A and S9A). Microglia from the V2L, ipsilateral and contralateral to the deprived eye, were extracted 5 days after 2wMD. We focused on seven genes previously implicated in morphological synapse plasticity: *Adam10* (a disintegrin and metalloprotease 10), *Bdnf* (brain-derived neurotrophic factor), *C1qa* (complement component 1, q subcomponent, A chain), *Gabbr1* (GABA$_B$ receptor subunit 1), *Tnf-α* (tumor necrosis factor alpha), *Mmp2* (matrix metalloproteinase 2), and *Mmp9*.[26,28–32] We hypothesized that the molecular changes associated with cross-modal plasticity would be primarily detected in the contralateral V2L. Only *C1qa* and *Mmp9* expression levels changed, both being upregulated in the contralateral V2L (Figures S6A and 7A). Both these genes are associated with the remodeling of synapses and spines. The matrix metalloproteinase (MMP) activity has been previously shown to facilitate microglial-mediated synapse elimination[33] and may facilitate microglial "stripping" of inhibitory synapses through digestion of the extracellular matrix. To test this hypothesis, we administered daily injections of the broad MMP inhibitor GM6001 (50 mg/kg, intraperitoneally, p10–p20; MD at p14, Figure 7B), a protocol previously shown to prevent MD-induced ocular dominance plasticity in V1.[34] In 2wMD mice, when MMPs were blocked (MMP9inh_2wMD), there was no clear subpopulation of V2L neurons that showed enhanced activity during complex whisker stimulation (Figure 7B). Besides, the frequency and amplitude of Ca^{2+} transients during rough and smooth sandpaper stimulation were significantly reduced compared with those in vehicle control 2wMD mice (Figures 7C and 7D, again for neurons with above-average basal activity). Daily local injection of a more specific MMP9 inhibitor directly into the V2L in 2wMD mice (MMP9inh[cortical injection]) (Figure S9B) similarly prevented the enhanced V2L excitability in response to sandpaper stimulation (Figures S9C and S9D). In addition, systemic MMP inhibition prevented the 2wMD-induced loss of V2L VGAT protein levels (Figures 7E and 7F) without affecting VGlut levels (Figures 7G and 7H). Our data suggest that MMP9 is a key molecular event mediating 2wMD-induced plasticity in the contralateral V2L.
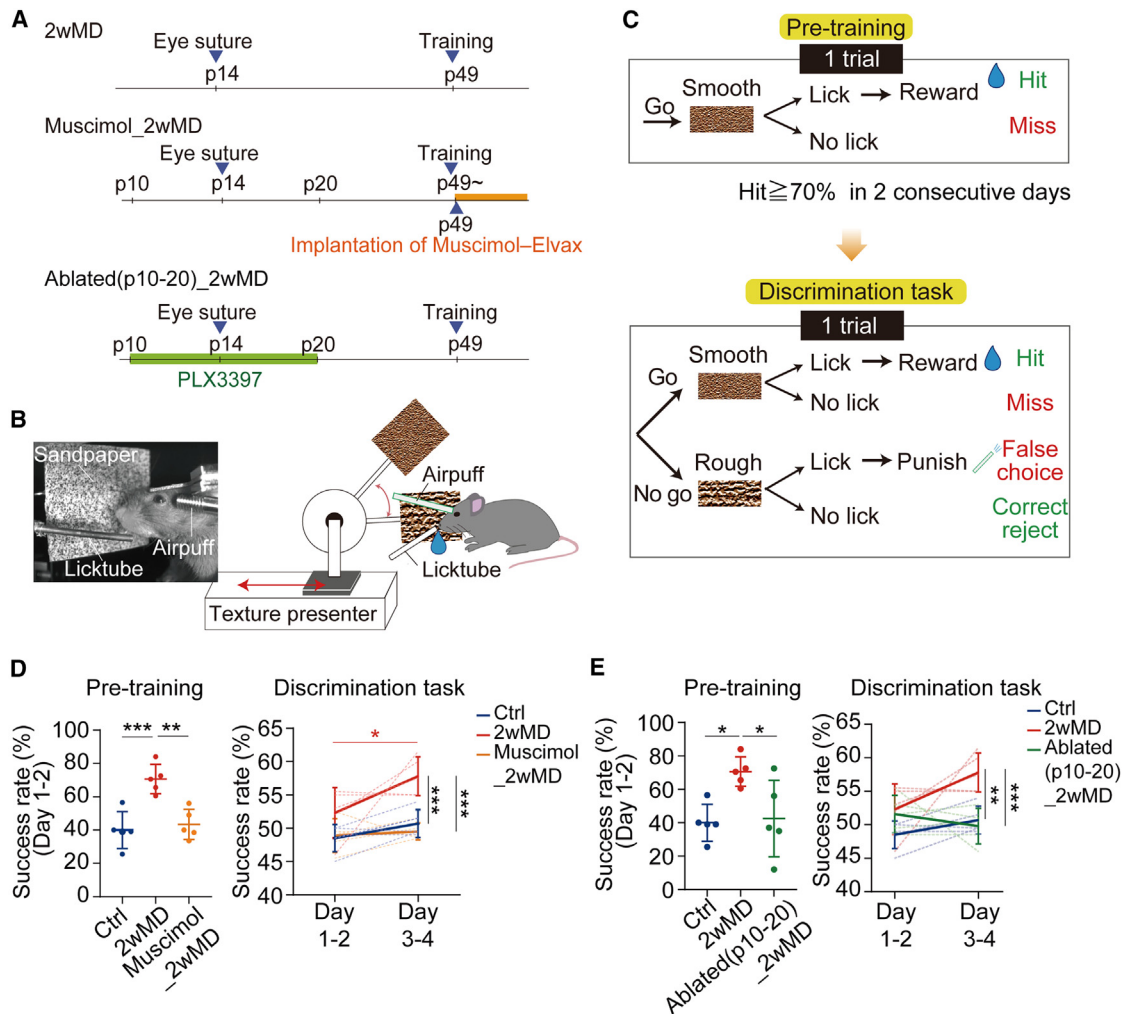
DISCUSSION

Two broad mechanisms may mediate the behavioral and neural adaptations seen after sensory deprivation:[35] "compensatory plasticity," whereby the spared somatosensory cortex may reorganize to enhance performance; and "cross-modal recruitment," whereby the deprived primary sensory cortices contribute

---

(E) Unitary EPSC amplitudes (uEPSCs) were similar in PV$^+$ neurons from control, 2wMD, and microglia-ablated mice. However, unitary IPSC (uIPSC) amplitudes were significantly smaller in 2wMD mice. On the other hand, 2wMD mice with microglia ablation did not show a decrease of uIPSC.

(F) There was no difference in the E/I ratio of S1bf-evoked EPSC amplitudes in pyramidal and PV$^+$ cells among the three groups.

(G) Scatterplots of the amplitude of synaptic currents in V2L Pyr neurons in response to S1bf afferent photostimulation and PV$^+$ neuron stimulation in control (n = 17 pairs) and 2wMD mice (n = 32 pairs). Regression lines show Pearson's correlation coefficients.

Figure 6. Monocular deprivation during the critical period increases the capacity for tactile discrimination

(A–C) Experimental protocol and scheme for the sensory discrimination task.

(D) 2wMD resulted in enhanced performance in the pre-training task, as measured by the higher success rate averaged over the first 2 days of training. This enhanced performance was not observed in the 2wMD mice wherein muscimol was locally eluted into the V2L. The 2wMD mice also showed a higher success rate in the discrimination task (measured as the sum of both Hit + Correct reject choices [see C], divided by total trials) averaged over days 3–4. Muscimol treatment also prevented this increase.
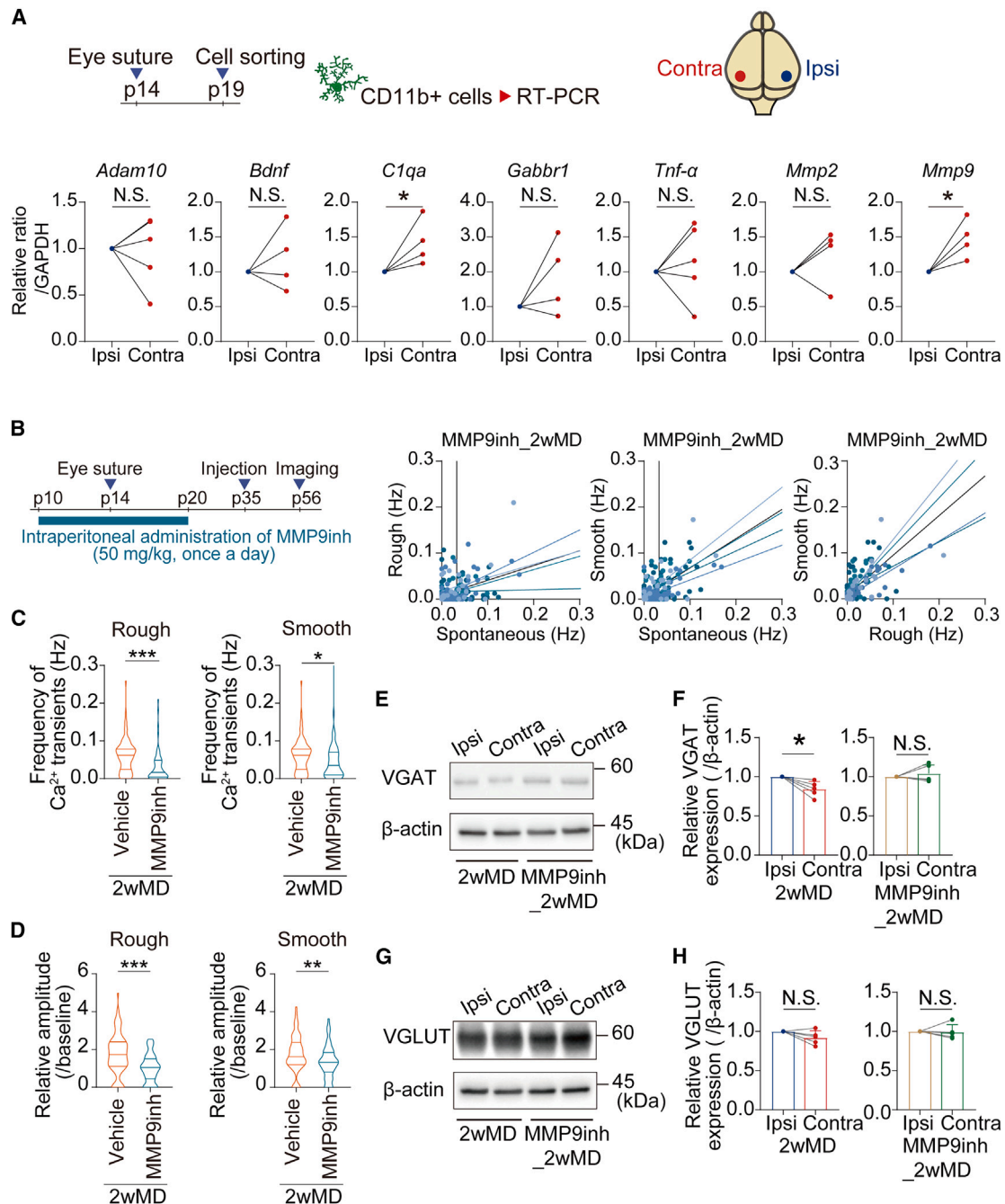
(E) 2wMD resulted in enhanced performance in the pre-training period, as measured by the higher success rate averaged over the first 2 days of training. This enhanced performance was not present in 2wMD mice with prior microglial ablation. The 2wMD mice also showed a higher success rate (measured as the sum of both Hit + Correct reject choices [see A], divided by total trials) averaged over days 3–4. Microglial ablation prevents this increase.

Data shown as mean ± SD.

---

to the enhanced sensory abilities. Our model suggests that cross-modal recruitment of the visual cortices is sufficient to subserve enhanced somatosensory behavior following critical-period MD. Manipulations that blocked the enhanced activity of V2L during whisker stimulation in 2wMD mice (i.e., microglia ablation, MMP9 inhibition, and muscimol treatment) also blocked enhanced tactile discrimination after MD. Similarly, activation of the occipital cortex in the blind (and in subjects with prolonged blindfolds) occurs during braille reading. Disruption of such increased visual cortex activity also impairs enhanced tactile performance.[8,36] Interestingly, little activation of the visual cortex was observed with simple finger tapping as opposed to braille

reading[37] and by analogy. Besides, we also observed enhanced V2L excitability with more complex patterns of whisker stimulation and not with simple whisker deflections, indicating that cross-modal plasticity may not be apparent with more passive stimulation models and requires physiologically relevant and perhaps more motivating stimuli in both rodents and humans.

The anatomical and functional connections between the primary and higher-order sensory cortices that contribute to cross-modal recruitment have been reported.[13,38] Our results confirm direct functional connections between the primary S1 barrel cortex and visual cortices, with the greatest density of terminations in the V2L. Connections to V2 from the primary

Figure 7. Inhibition of MMPs prevents 2wMD-induced plasticity

(A) RT-PCR analysis of structural plasticity genes in the V2L of 2wMD mice.

(B) Plot of the frequency of Ca^{2+} transients during basal conditions (spontaneous) and during whisker presentation with rough (upper) or smooth (middle) sandpaper for 2wMD mice treated with MMP inhibitor (MMP9inh_2wMD). Correlation between the frequency of V2L neuronal Ca^{2+} transients during rough and smooth sandpaper whisker stimulation in 2wMD mice with MMP inhibition (lower). Lines represent regression fits to data from individual mice (black line is the mean regression line).

(C and D) In 2wMD mice, MMP inhibition reduced the mean frequency (C) and amplitude (D) of Ca^{2+} transients seen during whisker stimulation, as compared with vehicle-treated mice.

(E) Representative western blot of VGAT protein expression levels in the ipsilateral and contralateral V2L of vehicle and MMP-inhibited 2wMD mice.

(F) Quantification of VGAT protein expression ratios in the contralateral V2L relative to the ipsilateral V2L, in 2wMD (left) and MMP-inhibited 2wMD (right) mice.

(G and H) VGlut relative expression levels were unaffected by either 2wMD by itself or with concurrent MMP inhibition.

Data shown as mean ± SD.

somatosensory and auditory cortices have been demonstrated in mice by tracing studies, either directly examined in V2 or noticeably adjacent to V1 sections.[22,38,39] We believe that this is the first report to visualize functional activity in direct S1bf-V2L connections. These connections were active during whisker stimulation, but the levels of afferent activity were the same in the control and 2wMD mice. We did not detect any increase in the extent of cross-cortical connectivity as reported for V1 after early binocular enucleation in opossums.[40] However, in a genetic model of severe visual impairment, an increase in cross-modal V1 responsiveness to whisker stimulation did not change corticocortical connections.[41] Increases in cross-modality cortical connections after sensory deprivation appear subtle and depend on the specific sense deprived, the timing of deprivation, and the examined species.[42,43] When we combined selective optogenetic stimulation and patch-clamp electrophysiology to assess the synaptic output of these S1bf-to-V2L connections, we observed no change after 2wMD. However, the local inhibitory circuits activated by S1bf stimuli were decreased. Use-dependent upscaling of synaptic efficacy has been suggested to contribute to cross-modal recruitment after sensory loss,[13,35] but we found no evidence of any increased efficacy within these S1bf-V2L pyramidal neuron synapses. Although we did not probe for changes in thalamocortical or other excitatory inputs, we suggest that the increased excitability of V2L neurons during complex sandpaper stimulation arises from the selective loss of local GABAergic inhibitory inputs. Simple whisker defects or optogenetic activation of the S1bf in normal mice evoke hyperpolarizing responses in V1 neurons through direct corticocortical projections.[44] Our results suggest that the loss of similar inhibitory responses in V2L unmasks cross-modal plasticity.

Microglia phagocytose these inhibitory synaptic inputs from local parvalbumin-positive GABAergic interneurons to V2L pyramidal neurons, adding to the repertoire of different physiological or pathological conditions under which microglia sculpt neural circuits.[45–48] Predominantly, microglia phagocytose excitatory synapses. However, this could be partially attributed to a bias reflecting a greater focus on the plasticity of glutamatergic connections. When specifically examined, microglia can also prune inhibitory synapses. Microglia activated by chronic lipopolysaccharide (LPS) injection were shown to "strip" GABAergic terminals off pyramidal neurons in the mouse motor cortex,[49] although this was reversible and actual phagocytosis of GABA puncta into microglial processes was not observed. More recently, microglia have been shown to phagocytose both inhibitory and excitatory cortical synapses during a critical developmental time window in early postnatal development, around p15–p17 in S1bf and during the subsequent week in V1.[32] As reported for synaptic pruning in developing lateral geniculate nucleus (LGN) pathways,[21] phagocytosed synapses were tagged with the complement cascade protein C1q. Genetic phenotyping and selective manipulation indicated that only a subset of microglia phagocytosed inhibitory terminals via a signaling cascade involving GABA$_B$ receptor subunits.[32] It seems reasonable that the same subpopulation of microglia targets the local inhibitory inputs within the V2L after MD, and a localized block of GABA signaling during a similar time window may prevent triggering of the cross-modal plasticity demonstrated in the study. A stron-

ger relative influence of S1 projection neurons in the face of silenced/deafferented visual projection neurons could result in more ambient GABA triggering responsive microglia to migrate around active neurons to initiate phagocytosis. However, other "find-me," "eat-me," and microglia motility signals are likely to be involved. In developing thalamic synapses of the visual system, less-active afferents express the complement cascade molecules C1q and C3, which identify them for phagocytosis by the C3 receptor expressed in microglia.[21,50] We also observed an increase in *C1qa* gene expression in V2L at 5 days after 2wMD, suggesting that this cascade is similarly involved. However, pruning of synapses in S1bf following whisker trimming is unaffected by the knockout of the C3 receptor. Instead, it involves chemokine signaling through fractalkine (CX3CL1) and its receptor (CX3CR1).[28] Interestingly, these results suggest that the secreted metalloprotease *Adam10* is required to initiate fractalkine signaling by cleaving the CX3CL1 ligand.[28] Our data showed no significant change in the expression levels of *Adam10* in the V2L following 2wMD. Rather, we showed that a different member of the large metalloprotease family, MMP9, was upregulated in the V2L after 2wMD. Microglial release of MMP9 can degrade components of the extracellular matrix, thereby facilitating the structural aspects of synaptic plasticity and their subsequent functional sequelae.[48] For example, ocular dominance and light reintroduction-induced plasticity in the V1 are attenuated in MMP-knockout mice. Hence, one possible scenario is that 2wMD causes microglia in the contralateral V2L to transition to a phenotype that releases MMP9. This degrades the extracellular matrix and/or perineuronal nets around pyramidal neurons that are targets of S1bf projections, thereby enabling greater contact between microglial processes and soma and/or proximal synapses. Eventually, these events trigger GABA detection and responsive microglia to initiate complement-dependent phagocytosis of PV$^+$ terminals. The 2wMD-induced changes in GABAergic neuronal activity may also facilitate microglial interactions via released ATP, which could then trigger microglial-mediated reductions in activity and subsequent tagging for phagocytosis.[51]

Our model of cross-modal plasticity represents a single manifestation of multisensory interactions. Animals constantly integrate simultaneous inputs from their senses to perceive their environment and enhance their performance. Models of such multisensory integration exist in both mice and humans.[18,52–54] Specific subcortical and "higher-order" cortical regions receive and integrate polymodal inputs, but more recently traditional "unimodal" cortical regions have been shown to respond to polymodal inputs. Sensory integration between these lower-order cortical regions enables faster processing and integration of intact sensory responses. The V2L in adult rats has been identified as one such region that integrates both audio and visual inputs.[55] The V2L is considered a logical integration area based on its location and identified projections from the primary audio and visual cortices.[18,55] Our results indicate that V2L also receives functional inputs from the S1bf and that it responds to MD with enhanced whisker-associated neuronal activity. Subsequently, this contributes to enhanced sensory discrimination seen after 2wMD. Therefore, it would be interesting to examine the role of the V2L in audio-tactile sensory integration in healthy rodents.

Multisensory integration is altered in autism spectrum disorder (ASD), and this has been replicated in mouse models of ASD symptoms for audiovisual and audio-tactile integration.[18,56] The ASD mouse model showed a reduced density of local PV$^+$ GABAergic puncta on pyramidal neurons within the insular cortex (where audio-tactile signals were integrated), and multisensory integration patterns were restored by the injection of the benzodiazepine diazepam. Further analogies have been drawn through the proposed contribution of MMP9 to neural and behavioral deficits in Fragile X syndrome, the most common genetic cause of ASD.[57] A deficit in local GABAergic signaling during a critical developmental period was proposed to result in multisensory impairments and ASD symptoms in mice.[56] Several genetic and post-translational changes in the molecules implicated in synaptic pruning are associated with ASD and other neurological diseases.[50] An intriguing possibility is that further understanding of how sensory experience and microglia regulate specific cross-cortical connections may provide therapeutic strategies for the treatment of these neurological disorders.

Limitations of the study

Probing the specific molecular elements of synaptic plasticity and their correlation with neural and behavioral measures is challenging. We recognize the limitations of the current study. Although we present strong evidence that microglial "stripping" of local inhibitory terminals in the V2L through MMP9-dependent mechanisms mediates the observed cross-modal plasticity, there are caveats and areas that we hope to resolve further. First, microglia play diverse roles throughout brain development, and ablation of microglia is a simple approach to probe specific aspects of their role in cross-modal plasticity. Indeed, we observed changes in V2L excitability, even when microglia were ablated in non-MD mice. Second, we aimed to identify the specific neural circuits in the V2L (and elsewhere) that participate in the enhanced behavioral somatosensory discrimination observed after MD. Almost all neurons in the slice responded to S1 stimulation, but presumably there are specific elements that are more important for the S1bf-V2L plasticity observed in our study. Our Ca^{2+} imaging did not provide a good indication of subthreshold activity, and we did not probe the temporal patterns of the V2L circuit activity before and after MD. Finally, the broader applications of this work could be extended by better mapping of different changes in microglia and neural circuits in neonatal vs. adult MD. Only MD was able to enhance discrimination ability during the critical period. Later, MD (p35) still impacted on V2L excitability. Developing approaches and tools to overcome these limitations could further add to our understanding of neural plasticity after injury or sensory loss and extend the potential value of the results reported here.

STAR★METHODS

Detailed methods are provided in the online version of this paper and include the following:

- KEY RESOURCES TABLE
- RESOURCE AVAILABILITY
  - Lead contact
  - Materials availability
  - Data and code availability
- EXPERIMENTAL MODEL AND SUBJECT DETAILS
- METHOD DETAILS
  - Surgery for MD or BD and *in vivo* imaging
  - Surgery for anterograde and retrograde tracing of cross-cortical neuronal projections
  - Pharmacological ablation of microglia and MMP inhibition
  - *In vivo* two-photon imaging during whisker stimulation
  - Image analysis
  - Histology
  - Image analysis after immunostaining
  - Real-time PCR
  - Immunoblotting
  - Sensory training and discrimination tasks
  - Electrophysiology
  - Serial block-face SEM
- QUANTIFICATION AND STATISTICAL ANALYSIS

REFERENCES

1. Hubel, D.H., and Wiesel, T.N. (1963). Receptive fields of cells in striate cortex of very young, visually inexperienced kittens. J. Neurophysiol. *26*, 994–1002. https://doi.org/10.1152/jn.1963.26.6.994.

2. Merzenich, M.M., Nelson, R.J., Stryker, M.P., Cynader, M.S., Schoppmann, A., and Zook, J.M. (1984). Somatosensory cortical map changes following digit amputation in adult monkeys. J. Comp. Neurol. *224*, 591–605. https://doi.org/10.1002/cne.902240408.

3. Lessard, N., Paré, M., Lepore, F., and Lassonde, M. (1998). Early-blind human subjects localize sound sources better than sighted subjects. Nature *395*, 278–280. https://doi.org/10.1038/26228.

4. Röder, B., Teder-Sälejärvi, W., Sterr, A., Rösler, F., Hillyard, S.A., and Neville, H.J. (1999). Improved auditory spatial tuning in blind humans. Nature *400*, 162–166. https://doi.org/10.1038/22106.

5. Goldreich, D., and Kanics, I.M. (2003). Tactile acuity is enhanced in blindness. J. Neurosci. *23*, 3439–3445.

6. Gougoux, F., Lepore, F., Lassonde, M., Voss, P., Zatorre, R.J., and Belin, P. (2004). Neuropsychology: pitch discrimination in the early blind. Nature *430*, 309. https://doi.org/10.1038/430309a.

7. Sadato, N., Pascual-Leone, A., Grafman, J., Ibañez, V., Deiber, M.P., Dold, G., and Hallett, M. (1996). Activation of the primary visual cortex by Braille reading in blind subjects. Nature *380*, 526–528. https://doi.org/10.1038/380526a0.

8. Cohen, L.G., Celnik, P., Pascual-Leone, A., Corwell, B., Falz, L., Dambrosia, J., Honda, M., Sadato, N., Gerloff, C., Catalá, M.D., and Hallett, M. (1997). Functional relevance of crossmodal plasticity in blind humans. Nature *389*, 180–183. https://doi.org/10.1038/38278.

9. Heimler, B., Weisz, N., and Collignon, O. (2014). Revisiting the adaptive and maladaptive effects of crossmodal plasticity. Neuroscience *283*, 44–63. https://doi.org/10.1016/j.neuroscience.2014.08.003.

10. Bavelier, D., and Neville, H.J. (2002). Cross-modal plasticity: where and how? Nat. Rev. Neurosci. *3*, 443–452. https://doi.org/10.1038/nrn848.

11. Nys, J., Scheyltjens, I., and Arckens, L. (2015). Visual system plasticity in mammals: the story of monocular enucleation-induced vision loss. Front. Syst. Neurosci. *9*, 60. https://doi.org/10.3389/fnsys.2015.00060.

12. Merabet, L.B., and Pascual-Leone, A. (2010). Neural reorganization following sensory loss: the opportunity of change. Nat. Rev. Neurosci. *11*, 44–52. https://doi.org/10.1038/nrn2758.

13. Teichert, M., and Bolz, J. (2018). How senses work together: cross-modal interactions between primary sensory cortices. Neural Plast. *2018*, 5380921. https://doi.org/10.1155/2018/5380921.

14. Lazzouni, L., and Lepore, F. (2014). Compensatory plasticity: time matters. Front. Hum. Neurosci. *8*, 340. https://doi.org/10.3389/fnhum.2014.00340.

15. Pascual-Leone, A., Amedi, A., Fregni, F., and Merabet, L.B. (2005). The plastic human brain cortex. Annu. Rev. Neurosci. *28*, 377–401. https://doi.org/10.1146/annurev.neuro.27.070203.144216.

16. Chen, R., Cohen, L.G., and Hallett, M. (2002). Nervous system reorganization following injury. Neuroscience *111*, 761–773. https://doi.org/10.1016/s0306-4522(02)00025-8.

17. Murphy, T.H., and Corbett, D. (2009). Plasticity during stroke recovery: from synapse to behaviour. Nat. Rev. Neurosci. *10*, 861–872. https://doi.org/10.1038/nrn2735.

18. Siemann, J.K., Veenstra-VanderWeele, J., and Wallace, M.T. (2020). Approaches to understanding multisensory dysfunction in autism spectrum disorder. Autism Res. *13*, 1430–1449. https://doi.org/10.1002/aur.2375.

19. Miyamoto, A., Wake, H., Ishikawa, A.W., Eto, K., Shibata, K., Murakoshi, H., Koizumi, S., Moorhouse, A.J., Yoshimura, Y., and Nabekura, J. (2016). Microglia contact induces synapse formation in developing somatosensory cortex. Nat. Commun. *7*, 12540. https://doi.org/10.1038/ncomms12540.

20. Paolicelli, R.C., Bolasco, G., Pagani, F., Maggi, L., Scianni, M., Panzanelli, P., Giustetto, M., Ferreira, T.A., Guiducci, E., Dumas, L., et al. (2011). Synaptic pruning by microglia is necessary for normal brain development. Science *333*, 1456–1458. https://doi.org/10.1126/science.1202529.

21. Schafer, D.P., Lehrman, E.K., Kautzman, A.G., Koyama, R., Mardinly, A.R., Yamasaki, R., Ransohoff, R.M., Greenberg, M.E., Barres, B.A., and Stevens, B. (2012). Microglia sculpt postnatal neural circuits in an activity and complement-dependent manner. Neuron *74*, 691–705. https://doi.org/10.1016/j.neuron.2012.03.026.

22. Laramée, M.E., Kurotani, T., Rockland, K.S., Bronchti, G., and Boire, D. (2011). Indirect pathway between the primary auditory and visual cortices through layer V pyramidal neurons in V2L in mouse and the effects of bilateral enucleation. Eur. J. Neurosci. *34*, 65–78. https://doi.org/10.1111/j.1460-9568.2011.07732.x.

23. Dreosti, E., Odermatt, B., Dorostkar, M.M., and Lagnado, L. (2009). A genetically encoded reporter of synaptic activity in vivo. Nat. Methods *6*, 883–889. https://doi.org/10.1038/nmeth.1399.

24. Madisen, L., Zwingman, T.A., Sunkin, S.M., Oh, S.W., Zariwala, H.A., Gu, H., Ng, L.L., Palmiter, R.D., Hawrylycz, M.J., Jones, A.R., et al. (2010). A robust and high-throughput Cre reporting and characterization system for the whole mouse brain. Nat. Neurosci. *13*, 133–140. https://doi.org/10.1038/nn.2467.

25. Elmore, M.R.P., Najafi, A.R., Koike, M.A., Dagher, N.N., Spangenberg, E.E., Rice, R.A., Kitazawa, M., Matusow, B., Nguyen, H., West, B.L., and Green, K.N. (2014). Colony-stimulating factor 1 receptor signaling is necessary for microglia viability, unmasking a microglia progenitor cell in the adult brain. Neuron *82*, 380–397. https://doi.org/10.1016/j.neuron.2014.02.040.

26. Stevens, B., Allen, N.J., Vazquez, L.E., Howell, G.R., Christopherson, K.S., Nouri, N., Micheva, K.D., Mehalow, A.K., Huberman, A.D., Stafford, B., et al. (2007). The classical complement cascade mediates CNS synapse elimination. Cell *131*, 1164–1178. https://doi.org/10.1016/j.cell.2007.10.036.

27. Grier, B.D., Belluscio, L., and Cheetham, C.E.J. (2016). Olfactory sensory activity modulates microglial-neuronal interactions during dopaminergic cell loss in the olfactory bulb. Front. Cell. Neurosci. *10*, 178. https://doi.org/10.3389/fncel.2016.00178.

28. Gunner, G., Cheadle, L., Johnson, K.M., Ayata, P., Badimon, A., Mondo, E., Nagy, M.A., Liu, L., Bemiller, S.M., Kim, K.W., et al. (2019). Sensory lesioning induces microglial synapse elimination via ADAM10 and fractalkine signaling. Nat. Neurosci. *22*, 1075–1088. https://doi.org/10.1038/s41593-019-0419-y.

29. Parkhurst, C.N., Yang, G., Ninan, I., Savas, J.N., Yates, J.R., Lafaille, J.J., Hempstead, B.L., Littman, D.R., and Gan, W.-B. (2013). Microglia promote learning-dependent synapse formation through brain-derived neurotrophic factor. Cell *155*, 1596–1609. https://doi.org/10.1016/j.cell.2013.11.030.

30. McCoy, M.K., and Tansey, M.G. (2008). TNF signaling inhibition in the CNS: implications for normal brain function and neurodegenerative disease. J. Neuroinflammation *5*, 45. https://doi.org/10.1186/1742-2094-5-45.

31. Zhao, H., Alam, A., Chen, Q., A Eusman, M., Pal, A., Eguchi, S., Wu, L., and Ma, D. (2017). The role of microglia in the pathobiology of neuropathic pain development: what do we know? Br. J. Anaesth. *118*, 504–516. https://doi.org/10.1093/bja/aex006.

32. Favuzzi, E., Huang, S., Saldi, G.A., Binan, L., Ibrahim, L.A., Fernández-Otero, M., Cao, Y., Zeine, A., Sefah, A., Zheng, K., et al. (2021). GABA-receptive microglia selectively sculpt developing inhibitory circuits. Cell *184*, 4048–4063.e32. https://doi.org/10.1016/j.cell.2021.06.018.

33. Uhm, J.H., Dooley, N.P., Villemure, J.G., and Yong, V.W. (1997). Mechanisms of glioma invasion: role of matrix-metalloproteinases. Can. J. Neurol. Sci. *24*, 3–15. https://doi.org/10.1017/s0317167100021028.

34. Pielecka-Fortuna, J., Kalogeraki, E., Fortuna, M.G., and Löwel, S. (2015). Optimal level activity of matrix metalloproteinases is critical for adult visual plasticity in the healthy and stroke-affected brain. Elife *5*, e11290. https://doi.org/10.7554/eLife.11290.

35. Lee, H.K., and Whitt, J.L. (2015). Cross-modal synaptic plasticity in adult primary sensory cortices. Curr. Opin. Neurobiol. *35*, 119–126. https://doi.org/10.1016/j.conb.2015.08.002.

36. Merabet, L.B., Hamilton, R., Schlaug, G., Swisher, J.D., Kiriakopoulos, E.T., Pitskel, N.B., Kauffman, T., and Pascual-Leone, A. (2008). Rapid and reversible recruitment of early visual cortex for touch. PLoS One *3*, e3046. https://doi.org/10.1371/journal.pone.0003046.

37. Gizewski, E.R., Gasser, T., de Greiff, A., Boehm, A., and Forsting, M. (2003). Cross-modal plasticity for sensory and motor activation patterns in blind subjects. Neuroimage *19*, 968–975. https://doi.org/10.1016/s1053-8119(03)00114-9.

38. Henschke, J.U., Noesselt, T., Scheich, H., and Budinger, E. (2015). Possible anatomical pathways for short-latency multisensory integration processes in primary sensory cortices. Brain Struct. Funct. *220*, 955–977. https://doi.org/10.1007/s00429-013-0694-4.

39. Van Brussel, L., Gerits, A., and Arckens, L. (2011). Evidence for cross-modal plasticity in adult mouse visual cortex following monocular enucleation. Cereb. Cortex *21*, 2133–2146. https://doi.org/10.1093/cercor/bhq286.

40. Karlen, S.J., Kahn, D.M., and Krubitzer, L. (2006). Early blindness results in abnormal corticocortical and thalamocortical connections. Neuroscience *142*, 843–858. https://doi.org/10.1016/j.neuroscience.2006.06.055.

41. Larsen, D.D., Luu, J.D., Burns, M.E., and Krubitzer, L. (2009). What are the effects of severe visual impairment on the cortical organization and connectivity of primary visual cortex? Front. Neuroanat. *3*, 30. https://doi.org/10.3389/neuro.05.030.2009.

42. Meredith, M.A., and Lomber, S.G. (2017). Species-dependent role of crossmodal connectivity among the primary sensory cortices. Hear. Res. *343*, 83–91. https://doi.org/10.1016/j.heares.2016.05.014.

43. Henschke, J.U., Oelschlegel, A.M., Angenstein, F., Ohl, F.W., Goldschmidt, J., Kanold, P.O., and Budinger, E. (2018). Early sensory experience influences the development of multisensory thalamocortical and intracortical connections of primary sensory cortices. Brain Struct. Funct. *223*, 1165–1190. https://doi.org/10.1007/s00429-017-1549-1.

44. Iurilli, G., Ghezzi, D., Olcese, U., Lassi, G., Nazzaro, C., Tonini, R., Tucci, V., Benfenati, F., and Medini, P. (2012). Sound-driven synaptic inhibition in primary visual cortex. Neuron *73*, 814–828. https://doi.org/10.1016/j.neuron.2011.12.026.

45. Wake, H., Moorhouse, A.J., Miyamoto, A., and Nabekura, J. (2013). Microglia: actively surveying and shaping neuronal circuit structure and function. Trends Neurosci. *36*, 209–217. https://doi.org/10.1016/j.tins.2012.11.007.

46. Ikegami, A., Haruwaka, K., and Wake, H. (2019). Microglia: lifelong modulator of neural circuits. Neuropathology *39*, 173–180. https://doi.org/10.1111/neup.12560.

47. Frost, J.L., and Schafer, D.P. (2016). Microglia: architects of the developing nervous system. Trends Cell Biol. *26*, 587–597. https://doi.org/10.1016/j.tcb.2016.02.006.

48. Crapser, J.D., Arreola, M.A., Tsourmas, K.I., and Green, K.N. (2021). Microglia as hackers of the matrix: sculpting synapses and the extracellular space. Cell. Mol. Immunol. *18*, 2472–2488. https://doi.org/10.1038/s41423-021-00751-3.

49. Chen, Z., Jalabi, W., Hu, W., Park, H.J., Gale, J.T., Kidd, G.J., Bernatowicz, R., Gossman, Z.C., Chen, J.T., Dutta, R., and Trapp, B.D. (2014). Microglial displacement of inhibitory synapses provides neuroprotection in the adult brain. Nat. Commun. *5*, 4486. https://doi.org/10.1038/ncomms5486.

50. Faust, T.E., Gunner, G., and Schafer, D.P. (2021). Mechanisms governing activity-dependent synaptic pruning in the developing mammalian CNS. Nat. Rev. Neurosci. *22*, 657–673. https://doi.org/10.1038/s41583-021-00507-y.

51. Badimon, A., Strasburger, H.J., Ayata, P., Chen, X., Nair, A., Ikegami, A., Hwang, P., Chan, A.T., Graves, S.M., Uweru, J.O., et al. (2020). Negative feedback control of neuronal activity by microglia. Nature *586*, 417–423. https://doi.org/10.1038/s41586-020-2777-8.

52. McGurk, H., and Macdonald, J. (1976). Hearing lips and seeing voices. Nature *264*, 746–748. https://doi.org/10.1038/264746a0.

53. Stein, B.E., and Stanford, T.R. (2008). Multisensory integration: current issues from the perspective of the single neuron. Nat. Rev. Neurosci. *9*, 255–266. https://doi.org/10.1038/nrn2331.

54. Yau, J.M., DeAngelis, G.C., and Angelaki, D.E. (2015). Dissecting neural circuits for multisensory integration and crossmodal processing. Philos. Trans. R. Soc. Lond. B Biol. Sci. *370*, 20140203. https://doi.org/10.1098/rstb.2014.0203.

55. Hirokawa, J., Bosch, M., Sakata, S., Sakurai, Y., and Yamamori, T. (2008). Functional role of the secondary visual cortex in multisensory facilitation in rats. Neuroscience *153*, 1402–1417. https://doi.org/10.1016/j.neuroscience.2008.01.011.

56. Gogolla, N., Takesian, A.E., Feng, G., Fagiolini, M., and Hensch, T.K. (2014). Sensory integration in mouse insular cortex reflects GABA circuit maturation. Neuron *83*, 894–905. https://doi.org/10.1016/j.neuron.2014.06.033.

57. Gantois, I., Khoutorsky, A., Popic, J., Aguilar-Valles, A., Freemantle, E., Cao, R., Sharma, V., Pooters, T., Nagpal, A., Skalecka, A., et al. (2017). Metformin ameliorates core deficits in a mouse model of fragile X syndrome. Nat. Med. *23*, 674–677. https://doi.org/10.1038/nm.4335.

58. Chen, T.-W., Wardill, T.J., Sun, Y., Pulver, S.R., Renninger, S.L., Baohan, A., Schreiter, E.R., Kerr, R.A., Orger, M.B., Jayaraman, V., et al. (2013). Ultrasensitive fluorescent proteins for imaging neuronal activity. Nature *499*, 295–300. https://doi.org/10.1038/nature12354.

59. Zhang, Y., Rózsa, M., Bushey, D., Zheng, J., Reep, D., Broussard, G.J., Tsang, A., Tsegaye, G., Patel, R., Narayan, S., et al. (2020). jGCaMP8 fast genetically encoded calcium indicators. https://janelia.figshare.com/articles/online_resource/jGCaMP8_Fast_Genetically_Encoded_Calcium_Indicators/13148243.

60. Tervo, D.G.R., Hwang, B.Y., Viswanathan, S., Gaj, T., Lavzin, M., Ritola, K.D., Lindo, S., Michael, S., Kuleshova, E., Ojala, D., et al. (2016). A designer AAV variant permits efficient retrograde access to projection neurons. Neuron *92*, 372–382. https://doi.org/10.1016/j.neuron.2016.09.021.

61. Oh, S.W., Harris, J.A., Ng, L., Winslow, B., Cain, N., Mihalas, S., Wang, Q., Lau, C., Kuan, L., Henry, A.M., et al. (2014). A mesoscale connectome of the mouse brain. Nature *508*, 207–214. https://doi.org/10.1038/nature13186.

62. Vezzoli, E., Caron, I., Talpo, F., Besusso, D., Conforti, P., Battaglia, E., Sogne, E., Falqui, A., Petricca, L., Verani, M., et al. (2019). Inhibiting pathologically active ADAM10 rescues synaptic and cognitive decline in Huntington's disease. J. Clin. Invest. *129*, 2390–2403. https://doi.org/10.1172/jci120616.

63. Zhu, C., Xu, J., Lin, Y., Ju, P., Duan, D., Luo, Y., Ding, W., Huang, S., Chen, J., and Cui, D. (2018). Loss of microglia and impaired brain-neurotrophic factor signaling pathway in a comorbid model of chronic pain and depression. Front. Psychiatry *9*, 442. https://doi.org/10.3389/fpsyt.2018.00442.

64. Fonseca, M.I., Chu, S.H., Hernandez, M.X., Fang, M.J., Modarresi, L., Selvan, P., MacGregor, G.R., and Tenner, A.J. (2017). Cell-specific deletion of C1qa identifies microglia as the dominant source of C1q in mouse brain. J. Neuroinflammation *14*, 48. https://doi.org/10.1186/s12974-017-0814-9.

65. Perea, G., Gómez, R., Mederos, S., Covelo, A., Ballesteros, J.J., Schlosser, L., Hernández-Vivanco, A., Martín-Fernández, M., Quintana,

R., Rayan, A., et al. (2016). Activity-dependent switch of GABAergic inhibition into glutamatergic excitation in astrocyte-neuron networks. Elife 5, e20362. https://doi.org/10.7554/eLife.20362.

66. Wang, K., Wang, H., Lou, W., Ma, L., Li, Y., Zhang, N., Wang, C., Li, F., Awais, M., Cao, S., et al. (2018). IP-10 promotes blood–brain barrier damage by inducing tumor necrosis factor alpha production in Japanese encephalitis. Front. Immunol. 9, 1148. https://doi.org/10.3389/fimmu.2018.01148.

67. Liou, J.T., Sum, D.C.W., Liu, F.C., Mao, C.C., Lai, Y.S., and Day, Y.J. (2013). Spatial and temporal analysis of nociception-related spinal cord matrix metalloproteinase expression in a murine neuropathic pain model. J. Chin. Med. Assoc. 76, 201–210. https://doi.org/10.1016/j.jcma.2012.12.011.

68. Hu, F., Ku, M.C., Markovic, D., Dzaye, O.D.a., Lehnardt, S., Synowitz, M., Wolf, S.A., and Kettenmann, H. (2014). Glioma-associated microglial MMP9 expression is upregulated by TLR2 signaling and sensitive to minocycline. Int. J. Cancer 135, 2569–2578. https://doi.org/10.1002/ijc.28908.

69. Haruwaka, K., Ikegami, A., Tachibana, Y., Ohno, N., Konishi, H., Hashimoto, A., Matsumoto, M., Kato, D., Ono, R., Kiyama, H., et al. (2019). Dual microglia effects on blood brain barrier permeability induced by systemic inflammation. Nat. Commun. 10, 5816. https://doi.org/10.1038/s41467-019-13812-z.

70. Tanahira, C., Higo, S., Watanabe, K., Tomioka, R., Ebihara, S., Kaneko, T., and Tamamaki, N. (2009). Parvalbumin neurons in the forebrain as revealed by parvalbumin-Cre transgenic mice. Neurosci. Res. 63, 213–223. https://doi.org/10.1016/j.neures.2008.12.007.

71. Sadahiro, M., Demars, M.P., Burman, P., Yevoo, P., Zimmer, A., and Morishita, H. (2020). Activation of somatostatin interneurons by nicotinic modulator Lypd6 enhances plasticity and functional recovery in the adult mouse visual cortex. J. Neurosci. 40, 5214–5227. https://doi.org/10.1523/jneurosci.1373-19.2020.

72. Kato, D., Wake, H., Lee, P.R., Tachibana, Y., Ono, R., Sugio, S., Tsuji, Y., Tanaka, Y.H., Tanaka, Y.R., Masamizu, Y., et al. (2020). Motor learning requires myelination to reduce asynchrony and spontaneity in neural activity. Glia 68, 193–210. https://doi.org/10.1002/glia.23713.

73. Conte, W.L., Kamishina, H., and Reep, R.L. (2009). The efficacy of the fluorescent conjugates of cholera toxin subunit B for multiple retrograde tract tracing in the central nervous system. Brain Struct. Funct. 213, 367–373. https://doi.org/10.1007/s00429-009-0212-x.

74. Li, M., Li, Z., Ren, H., Jin, W.N., Wood, K., Liu, Q., Sheth, K.N., and Shi, F.D. (2017). Colony stimulating factor 1 receptor inhibition eliminates microglia and attenuates brain injury after intracerebral hemorrhage. J. Cereb. Blood Flow Metab. 37, 2383–2395. https://doi.org/10.1177/0271678x16666551.

75. Lin, C., Wu, W., Lu, H., Li, W., Bao, Z., Wang, Y., Zhao, L., Guo, T., Cai, N., Li, Z., et al. (2021). MMP-9 Inhibitor GM6001 prevents the development of ssTBI-induced Parkinson's disease via the autophagy pathway. Cell. Mol. Neurobiol. 41, 1651–1663. https://doi.org/10.1007/s10571-020-00933-z.

76. Gursoy-Ozdemir, Y., Qiu, J., Matsuoka, N., Bolay, H., Bermpohl, D., Jin, H., Wang, X., Rosenberg, G.A., Lo, E.H., and Moskowitz, M.A. (2004). Cortical spreading depression activates and upregulates MMP-9. J. Clin. Invest. 113, 1447–1455. https://doi.org/10.1172/JCI21227.

77. Underly, R.G., Levy, M., Hartmann, D.A., Grant, R.I., Watson, A.N., and Shih, A.Y. (2017). Pericytes as inducers of rapid, matrix metalloproteinase-9-dependent capillary damage during ischemia. J. Neurosci. 37, 129–140. https://doi.org/10.1523/jneurosci.2891-16.2016.

78. Thévenaz, P., Ruttimann, U.E., and Unser, M. (1998). A pyramid approach to subpixel registration based on intensity. IEEE Trans. Image Process. 7, 27–41. https://doi.org/10.1109/83.650848.

79. Giovannucci, A., Friedrich, J., Gunn, P., Kalfon, J., Koay, S.A., Taxidis, J., Najafi, F., Gauthier, J.L., Zhou, P., Tank, D.W., et al. (2018). CalmAn: an open source tool for scalable Calcium Imaging data Analysis. Preprint at bioRxiv. https://doi.org/10.1101/339564.

80. Pachitariu, M., Stringer, C., Schröder, S., Dipoppa, M., Rossi, L.F., Carandini, M., and Harris, K.D. (2016). Suite2p: beyond 10,000 neurons with standard two-photon microscopy. Preprint at bioRxiv. https://doi.org/10.1101/061507.

81. Okada, T., Kato, D., Nomura, Y., Obata, N., Quan, X., Morinaga, A., Yano, H., Guo, Z., Aoyama, Y., Tachibana, Y., et al. (2021). Pain induces stable, active microcircuits in the somatosensory cortex that provide a therapeutic target. Sci. Adv. 7, eabd8261. https://doi.org/10.1126/sciadv.abd8261.

82. Dunn, K.W., Kamocka, M.M., and McDonald, J.H. (2011). A practical guide to evaluating colocalization in biological microscopy. Am. J. Physiol. Cell Physiol. 300, C723–C742. https://doi.org/10.1152/ajpcell.00462.2010.

83. Chen, J.L., Carta, S., Soldado-Magraner, J., Schneider, B.L., and Helmchen, F. (2013). Behaviour-dependent recruitment of long-range projection neurons in somatosensory cortex. Nature 499, 336–340. https://doi.org/10.1038/nature12236.

84. Chéreau, R., Bawa, T., Fodoulian, L., Carleton, A., Pagès, S., and Holtmaat, A. (2020). Dynamic perceptual feature selectivity in primary somatosensory cortex upon reversal learning. Nat. Commun. 11, 3245. https://doi.org/10.1038/s41467-020-17005-x.

85. Hayar, A., Bryant, J.L., Boughter, J.D., and Heck, D.H. (2006). A low-cost solution to measure mouse licking in an electrophysiological setup with a standard analog-to-digital converter. J. Neurosci. Methods 153, 203–207. https://doi.org/10.1016/j.jneumeth.2005.10.023.

86. Narushima, M., Yagasaki, Y., Takeuchi, Y., Aiba, A., and Miyata, M. (2019). The metabotropic glutamate receptor subtype 1 regulates development and maintenance of lemniscal synaptic connectivity in the somatosensory thalamus. PLoS One 14, e0226820. https://doi.org/10.1371/journal.pone.0226820.

87. Thai, T.Q., Nguyen, H.B., Sui, Y., Ikenaka, K., Oda, T., and Ohno, N. (2019). Interactions between mitochondria and endoplasmic reticulum in demyelinated axons. Med. Mol. Morphol. 52, 135–146. https://doi.org/10.1007/s00795-018-0212-0.

88. Alan, P., Sanford, L.P., and Henry, deF. (1991). The Fine Structure of the Nervous System: The Neurons and Supporting Cells (Oxford University Press).

89. Peters, A., Palay, S.L., and Webster, H.deF. (1991). The Fine Structure of the Nervous System: Neurons and Their Supporting Cells.

CellPress
OPEN ACCESS

STAR★METHODS

KEY RESOURCES TABLE

REAGENT or RESOURCE	SOURCE	IDENTIFIER
Antibodies		
Goat polyclonal anti-Iba1	Abcam	Cat#ab5076 RRID: AB_2224402
Rat monoclonal anti-CD68	Bio-Rad	Cat# MCA1957GA RRID: AB_324217
Rabbit monoclonal anti-C1q	Abcam	Cat#ab182451 RRID: AB_2732849
Mouse monoclonal anti-NeuN	Sigma-Aldrich	Cat# MAB377 RRID: AB_2298772
Rabbit polyclonal anti-Parvalbumin	Abcam	Cat# ab11427 RRID: AB_298032
Guinea pig polyclonal anti-VGLUT1	Synaptic Systems	Cat#135 304 RRID: AB_887878
Guinea pig polyclonal anti-VGLUT2	Merck	Cat#32160702 RRID: AB_2665454
Rabbit polyclonal anti-VGAT	Synaptic Systems	Cat#131 002 RRID: AB_887871
Guinea pig polyclonal anti-VGAT	Synaptic Systems	Cat#131 004 RRID: AB_887873
Rabbit polyclonal anti-βactin	Abcam	Cat# ab8227 RRID: AB_2305186
Chicken polyclonal anti-GFP	NOVUS	Cat# NB100-1614 RRID: AB_10001164
Rat monoclonal anti-m2AchR	Sigma-Aldrich	Cat# MAB367 RRID: AB_94952
Donkey polyclonal anti-goat Alexa 488	Abcam	Cat# ab150129 RRID: AB_2687506
Donkey polyclonal anti-rabbit Alexa 594	Abcam	Cat# ab150076 RRID: AB_2782993
Donkey anti-mouse Alexa 405	Abcam	Cat# ab175658 RRID: AB_2687445
Donkey polyclonal anti-guinea pig Alexa 647	Jackson Immuno-Research Labs	Cat# 706-605-148 RRID: AB_2340476
Goat polyclonal anti-rat Alexa 555	Invitrogen	Cat# A2134 RRID: AB_141733
Donkey polyclonal anti-mouse Alexa 647	Abcam	Cat# ab150107 RRID: AB_2890037
Goat anti-chicken IgY H&L Alexa 488	Abcam	Cat# ab150169 RRID: AB_2636803
CD11b (Microglia) MicroBeads, human and mouse	Miltenyi Biotec	Cat#130-093-634
Donkey polyclonal HRP-conjugated anti-rabbit	Invitrogen	Cat#31458 RRID: AB_228213
Rabbit polyclonal HRP-conjugated anti-guinea pig	Invitrogen	Cat# PA1-28597 RRID: AB_10981814
Bacterial and virus strains		
AAV1-hSyn-GCaMP6f-WPRE-SV40	Chen et al.[58]	Addgene #100837-AAV1
AAV1-hSyn-GCaMP8s-WPRE-SV40	Zhang et al.[59]	Addgene #162374-AAV1

(Continued on next page)

Continued

REAGENT or RESOURCE	SOURCE	IDENTIFIER
AAV1-CAG-flex-GCaMP6f-WPRE-SV40	Chen et al.[58]	Addgene #100835-AAV1
AAV1-hSyn-hChR2(H134R)-EYFP	Karl Deisseroth	Addgene #26973-AAV1
AAV1-hSyn-eGFP-WPRE-bGH	Bryan Roth	Addgene #50465-AAV1
pENN.AAV.CamKII 0.4.Cre.SV40	James M. Wilson	Addgene #105558-plasmid
rAAV2-retro helper	Tervo et al.[60]	Addgene #81070-plasmid
pAAV1-CAG-flex-eGFP-WPRE	Oh et al.[61]	Addgene #51502-plasmid
Alexa-Fluor-488-conjugated cholera toxin subunit B	Invitrogen	Cat# C34775
Chemicals, peptides, and recombinant proteins		
Pexidartinib (PLX 3397)	MedChemExpress	Cat# HY-16749 CAS: 1029044-16-3
Pexidartinib	Chemgood	Cat#C-1271
GM6001	Cayman Chemical	CAS: 142880-36-2
4-Aminopyridine (4-AP)	Abcam	CAS: 504-24-5
Tetrodotoxin (TTX)	FUJIFILM	CAS: 4368-28-9
MMP-9 inhibitor I	Sigma-Aldrich	CAS: 1177749-58-4
Muscimol hydrobromide	Sigma-Aldrich	CAS: 18174-72-6
Critical commercial assays		
Pierce™ BCA Protein Assay Kit	Thermo Scientific	Cat#23225
Experimental models: Organisms/strains		
Mouse: C57BL/6J	The Jackson Laboratory	JAX: 00066 RRID: IMSR_JAX:000664
Mouse: B6; 129P2-Pvalb$^{tm1(cre)Arbr}$/J	The Jackson Laboratory	JAX: 008069 RRID: IMSR_JAX:017320
Mouse: B6.Cg-Gt(ROSA)26Sor$^{tm14(CAG-tdTomato)Hze}$/J	The Jackson Laboratory	JAX: 007914 RRID: IMSR_JAX:007909
Mouse: B6N.Cg-Sst$^{tm2.1(cre)Zjh}$/J	The Jackson Laboratory	JAX: 018973 RRID: IMSR_JAX:018973
Oligonucleotides		
Primer: *Adam10* Forward: GGAAGCTTTAGTCATGGGTCTG	Vezzoli et al.[62]	N/A
Primer: *Adam10* Reverse: CTCCTTCCTCTACTCCAGTCAT	Vezzoli et al.[62]	N/A
Primer: *Bdnf* Forward: TCGGTTGCATGAAGGC	Zhu et al.[63]	N/A
Primer: *Bdnf* Reverse: GTTTTCTTCGTTGGGC	Zhu et al.[63]	N/A
Primer: *C1qa* Forward: CTCAGGGATGGCTGGTGGCC	Fonseca et al.[64]	N/A
Primer: *C1qa* Reverse: CCTTTGAGACCCGGCCTCCCC	Fonseca et al.[64]	N/A
Primer: *Gabbr1* Forward: CGAAGCATTTCCAACATGAC	Perea et al.[65]	N/A
Primer: *Gabbr1* Reverse: CAAGGCCCAGATAGCATCATA	Perea et al.[65]	N/A
Primer: *Tnf-α* Forward: TCACTGGAGCCTCGAATGTC	Wang et al.[66]	N/A

(Continued on next page)

Continued

REAGENT or RESOURCE	SOURCE	IDENTIFIER
Primer: *Tnf-α* Reverse: GTGAGGAAGGCTGTGCATTG	Wang et al.[66]	N/A
Primer: *Mmp2* Forward: GTCTTTGATGGCATCGCTCAG	Liou et al.[67]	N/A
Primer: *Mmp2* Reverse: GGCCTCATACACAGCGTCAAT	Liou et al.[67]	N/A
Primer: *Mmp9* Forward: CATTCGCGTGGATAAGGAGT	Hu et al.[68]	N/A
Primer: *Mmp9* Reverse: ACCTGGTTCACCTCATGGTC	Hu et al.[68]	N/A
Primer: *Gapdh* Forward: AATGCATCCTGCACCACCAAC	Haruwaka et al.[69]	N/A
Primer: *Gapdh* Reverse: TGGATGCAGGGATGATGTTCTG	Haruwaka et al.[69]	N/A
Software and algorithms		
ImageJ	National Institutes of Health	https://imagej.nih.gov/ij/
Fiji (Fiji Is Just ImageJ)	Open source	https://imagej.net/software/fiji/
MATLAB	MathWorks	https://www.mathworks.com/products/matlab.html
LabVIEW	National Instruments	https://www.ni.com/en-gb/shop/labview.html
LightCycler 96 System	Roche Diagnostics	N/A
Fusion-Capt Advance Software version Solo 7 17.00d	Vilber Lourmat	N/A
GraphPad Prism 8	GraphPad Software Inc	https://www.graphpad.com/scientific-software/prism/
iBright™ CL1500 Imaging System	Thermo Scientific	N/A
Imaris	Oxford Instruments	https://imaris.oxinst.com/
pClamp9	Molecular Devices	N/A
Other		
Two-photon microscope	Carl Zeiss	LSM 7 MP system
NIR laser (for two-photon microscope)	Spectra-Physics	Mai Tai HP
NIR laser (for two-photon microscope)	Spectra-Physics	Mai Tai DeepSee
Two-photon microscope	Nikon	A1MP system
NIR laser (for two-photon microscope)	Spectra-Physics	InSight X3
10× water immersion objective	Carl Zeiss	Plan-APOCHROMAT
16× water immersion objective	Nikon	N16XLWD-PF
25× water immersion objective	Nikon	N25X-APO-MP
Fluorescence microscope unit	Keyence	BZ-X700
Confocal microscope unit	Keyence	Zeiss LSM510 Meta
Confocal microscope unit	Olympus	FV3000
20× objective	Carl Zeiss	Plan-APOCHROMAT
63× oil immersion objective	Carl Zeiss	EC Plan-NEOFLUAR
10× water immersion objective	Olympus	LUMPlanFl
Vibratome	Campden Instruments	5100 mz
Microtome	Leica Microsystems	SM2010 R
Motorized linear stage	Zaber	T-LSM100A
Piezo-electric stepper	Physik Instrument	PL140.11
Sandpaper	KAKURI Sangyo	# 80 (rough)
Sandpaper	KAKURI Sangyo	# 400 (smooth)

RESOURCE AVAILABILITY

Lead contact

Further information and requests for resources and reagents should be directed to and will be fulfilled by the lead contact, Hiroaki Wake (hirowake@med.nagoya-u.ac.jp).

Materials availability

This study did not generate unique reagents.

Data and code availability

- All data reported in this paper will be shared by the lead contact upon request.
- This paper does not report original code.
- Any additional information required to reanalyze the data reported in this paper is available from the lead contact upon request.

EXPERIMENTAL MODEL AND SUBJECT DETAILS

All experimental protocols were approved by the Animal Care and Use Committees of the Kobe University Graduate School of Medicine, Osaka University Graduate School of Medicine, and Nagoya University Graduate School of Medicine. The study protocol was conducted in accordance with the National Institute of Health Guide for the Care and Use of Laboratory Animals. Male mice were used for most of the experiments, except for SST-Cre mice (full denomination: B6N.Cg-S$^{sttm2.1(cre)Zjh}$/J, RRID: IMSR_JAX:018973), to avoid potential variability resulting from estrus cycles. All mice were allowed free access to food and water (unless otherwise specified for behavioral assays) and housed under a 12 h light/dark cycle, unless otherwise specified. For *in vivo* Ca^{2+} imaging, we used C57BL/6 (WT) mice, PV-Cre mice (full denomination: B6.129P2-Pvalb$^{tm1(cre)Arbr}$/J, RRID: IMSR_JAX:017320)[70] and SST-Cre mice. Electrophysiological experiments and two-photon imaging were used to identify the V2L in mice derived from crossing PV-Cre mice and Rosa26-tdTomato reporter mice (Ai14) (full denomination: B6.Cg-Gt(ROSA)26Sor$^{tm9(CAG-tdTomato)Hze}$/J, RRID: IMSR_JAX:007909),[24] both derived from the C57BL/6J strain. Monocular/Binocular deprivation was done in p14 for 2wMD and 2wBD mice, and in p35 for 5wMD mice. The administration of PLX3397, GM6001, MMP-9 inhibitor I, and DMSO administration was done in p1-p10 (Figures S5A–S5C), in p10-p19 (Figures 4, 7A, and 7E–7H), in p10-p20 (Figures 3, 5, 6, 7B–7D, S5J–S5L, and S9B–S9D), in p31-p41 (Figures S5G–S5I) or in p35-p45 (Figures S5D–S5F). Virus injection was performed in p35 (Figures 1, 2, 3, 7, S1, S2C, S3, S4, S5A–S5F, S5J–S5L, and S9) or in p56 (Figures S2D–S2G and S5G–S5I) and following Ca^{2+} imaging was performed 3–4 weeks later. For Ca^{2+} imaging in developmental stage, virus injection was performed in p2 and imaging was performed in p21 and p41 (Figures S2A and S2B). Alexa-488 CTB injection was performed in p35. Perfusion (and fixation) was performed in p17 (Figure S6B), p19 (Figures 4, S6A, S6C, and 7), p40 (Figure S9A), 6-weeks (Figures 1D–1F), 8weeks (Figures 1A–1C and S1). For electrophysiology, virus injection was performed in p21, followed by perfusion for slice patch in p35. For sensory training and discrimination tasks, training was started in p49 (Figures 6 and S8A–S8C) and p56 (Figures S8D–S8F). The implantation of muscimol-Elvax was performed on the beginning day of the training.

METHOD DETAILS

Surgery for MD or BD and *in vivo* imaging

Mice were monocularly deprived at postnatal day (p) 14 or p35 by suturing the lid of the right eye and/or binocularly deprived at p14 by suturing the lid of both eyes under isoflurane anesthesia (1-4% v/vol in O$_2$). This area was contralateral to the left secondary lateral visual cortex (V2L) used for imaging, as described below. The upper and lower lids were slightly trimmed, then sutured together and further sealed using Vetbond (3M, St Paul, Minnesota).[71] Surgery for subsequent imaging was performed for both control and MD mice.[72] Under anesthesia with ketamine (74 mg/kg, *i.p.*) and xylazine (10 mg/kg, *i.p.*), the skin was disinfected with 70% (w/v) ethanol, the skull was exposed and cleaned, and a custom-made headplate was firmly attached to the skull using dental cement (G-CEM ONE; GC, Tokyo, Japan). The intact skull surface was coated with an acrylic-based dental adhesive resin cement (Super bond; Sun Medical, Shiga, Japan) to avoid drying. This head plate allowed secure attachment of the mouse to a stainless-steel frame to facilitate circular craniotomy surgery. This was followed by two-photon imaging.[69] Two days after the head-plate surgery, a circular craniotomy (2.5 mm diameter) was performed under isoflurane (1%) anesthesia over the left V2L (centered at 2.8 mm posterior and 3.8 mm lateral from bregma). At this stage, 1 μL recombinant adeno-associated virus (AAV) encoding the calcium-indicator protein, GCaMP6f, was pressure injected at three sites into layer 2/3 (L2/3, depth:150–200 μm below the cortical surface) using a glass pipette (tip diameter, 10 μm). AAV was injected into p2 of the left cortex. We used AAV1-hSyn-GCaMP6f-WPRE-SV40 (Addgene; 9.0 × 10^{12} vector genomes/mL, diluted 1:1 in phosphate-buffered saline [PBS]) as the AAV vector solution to visualize neuronal activity in large excitatory neurons or AAV1-CAG-flex-GCaMP6f-WPRE-SV40 (Addgene; 1.0 × 10^{13} vector genomes/mL, diluted 1:1 in PBS) to visualize GABAergic neuronal activity in PV-Cre[58] and SST-Cre mice. For *in vivo* imaging of axons projecting from the left S1bf, we injected AAV1-hSyn-GCaMP8s-WPRE-SV40 (Addgene; 9.0 × 10^{12} vector genomes/mL, diluted 1:1 in PBS, total volume

1 μL) at three sites in the left S1bf at a similar depth (centered at 1.5 mm posterior and 3.0 mm lateral from bregma). Subsequently, the brain surface within the cranial window was covered with 2% (w/v) agarose L (Nippon Gene, Tokyo, Japan) mixed in saline and a glass window composed of two coverslips with diameters of 2.0 and 4.5 mm, respectively (Matsunami Glass, Osaka, Japan).[69] These were joined using an ultraviolet curable adhesive (NOR-61, Norland). The cranial window edges were sealed using dental cement combined with a dental adhesive resin cement (Super Bond; Sun Medical, Shiga, Japan). Following surgery, the mice were recovered and individually housed while awaiting imaging experiments, 3-4 weeks later.

Surgery for anterograde and retrograde tracing of cross-cortical neuronal projections

Regarding anterograde tracing of direct projections from the S1 to V2L, AAV1-Syn-eGFP (Addgene; 1.2×10^{13} vector genomes/mL, volume 1 μL) was injected at two sites in the left S1 cortex at a depth of 300 μm below the cortical surface. For retrograde tracing, Alexa-Fluor-488-conjugated cholera toxin subunit B (Alexa 488-CTB; 0.1% solution in PBS, volume 1 μL, Invitrogen) was pressure-injected into the five-week-old control and MD mice at two sites in the V2L.[73] For retrograde tracing by AAV, AAVretro-CamKII-cre (2.93×10^{12} vector genomes/ml, volume 1 μL) was injected at two sites in the left V2L cortex at a depth of 100, 300 and 500 μm below the cortical surface and AAV1-CAG-flex-eGFP (2.88×10^{13} vector genomes/ml, volume 1 μL) was injected at one site in the left S1bf. Fluorescence intensity was analyzed using ImageJ (National Institutes of Health, Bethesda, MD, USA) at one week (Alexa 488-CTB injection) or three weeks (AAV1-Syn-eGFP) after injection.

Pharmacological ablation of microglia and MMP inhibition

Microglia were ablated using pharmacological inhibition of the colony-stimulating factor 1 receptor by oral dosing of PLX 3397 (75 mg/kg; MedChemExpress, USA) given as twice-daily gavage 7.5 mg/mL PLX 3397 diluted in 3.75% dimethyl sulfoxide and 1% polyoxyethylene (20) sorbitan monolaurate in saline to a total volume of 40-80 μL. This was administered from postnatal days 10 to 20[25,74] or by oral administration of PLX 3397 containing feed (290 mg/kg, Research Diets, USA). Vehicle control mice were administered the same volume of PLX-free mixture twice daily by gavage. To inhibit MMPs, we administered GM6001 (50 mg/kg; Cayman Chemical, USA) as intraperitoneal injection (2.5 mg/mL GM6001 diluted in 3% dimethyl sulfoxide and 2% cyclodextrin in saline to a total volume of 80-160 μL) once a day from postnatal days 10 to 20.[34,75,76] For more specific inhibition of MMP9, we injected 0.02 pmol MMP-9 inhibitor I (Calbiochem) into the left V2L once per day from p10-p20.[77]

In vivo two-photon imaging during whisker stimulation

Three weeks after virus injection, two-photon images of the left (contralateral) V2L region were acquired using a laser scanning microscope (LSM 7 MP system; Carl Zeiss, Oberkochen, Germany, A1MP system; Nikon, Japan) with three water-immersion objective lenses (10×, numerical aperture [N.A.] 0.5 [Carl Zeiss] and 16×, N.A. 0.8 [Nikon] for soma imaging; 25×, N.A. 1.1 for axon imaging; Carl Zeiss) and a Ti: sapphire laser (Mai Tai HP, Mai Tai DeepSee and Insight X3; Spectra-Physics, Santa Clara, CA) operating at a 950-nm wavelength. The fields for soma imaging were 424.27 μm × 424.27 μm (2.0× digital zoom), while those for axon imaging were 141.42 μm × 141.42 μm (3.0× digital zoom), both at a depth of 150200 μm and 40–100 μm below the cortical surface for soma and axon imaging, respectively. The pixel size was 0.828 μm and 0.276 μm for soma and axon imaging, respectively. The duration of each imaging frame was 242 ms, and continuous sequential 1000-frame images were acquired continuously during whisker stimulation.

We used the following whisker stimulation protocols:1) brushing of rough (# 80) or smooth sandpaper (# 400, Kakuri Sangyo, Niigata, Japan) across the whiskers 10 Hz for 1 s, repeating this process five times over 242 s (Figures 2A–2F, 3D–3F, 7B–7D, S1J–S1L, S2H, S2, S3G–S3L, S4, and S5), back-and-forth movements of a glass pipette across the whiskers at 10 Hz over 1 sec, repeated five times (Figures 1G–1J, Figures S1D–S1I, and S3A–S3F tip diameter, 10 μm) using a piezo-electric stepper (PL140.11, Physik Instrument, Japan).

Image analysis

Image analysis was performed using ImageJ (National Institutes of Health, Bethesda, MD) and MATLAB (MathWorks, Natick, MA) software packages. Movies and 3D images were corrected for focal plane displacement using the ImageJ plug-in TurboReg and StackReg.[78] To estimate axon or neuronal activity in the V2L, we determined regions of interest (ROIs) using an automated algorithm (http://github.com/simonsfoundation/CaImAn)[79] or (https://github.com/MouseLand/suite2p)[80] that defines ROIs as discrete regions showing a change in fluorescence during analysis. Completely silent neurons or axonal boutons (and/or those without GCaMP6f or GCaMP6s expression) were not detected by this automated approach. We defined the baseline Ca^{2+} fluorescence (F_0) as the 35th percentile of the fluorescence intensity histogram obtained during the entire imaging period. Traces were calculated as $\Delta F/F_0$ ($\Delta F = F\text{-}F_0$), where F is the instantaneous fluorescent signal. We defined Ca^{2+} transients as ΔF exceeded 2 standard deviations of F_0. Ca^{2+} transient frequency was the division of the total number of transients by the imaging periods.[81] The amplitude was the average of peak $\Delta F/F_0$ of each Ca^{2+} transient. The correlation coefficients between the Ca^{2+} transients in two neurons during imaging were quantified using Pearson's correlation. This represented the homogeneity of the neuronal activity in the scale of -1(strong negative correlation) to 1 (strong positive correlation). Additionally, we examined the temporal coupling between neuronal activity and whisker stimulation through cross-correlation analysis (Figures 1H–1K, S1H, S1I, and S3C–S3F; xcorr, MATLAB) by measuring the correlation of the signal vector ($\Delta F/F_0$) from each ROI with vectors from the whisker simulation trajectory during the same imaging period (for Figures 1I and 1J) and within 48.4 sec (200 imaging frame durations) around each stimulation period (for Figures S1G, S1H,

S3D, and S3E). In cases where the lag of the xcorr peak was 0–1,210 s (five imaging frame durations), we defined neuronal activity as that coupled to the whisker stimulations.

Histology

Mice were deeply anesthetized using ketamine (74 mg/kg, *i.p.*) and xylazine (10 mg/kg, *i.p.*) and then transcardially perfused with a 4% paraformaldehyde solution in PBS. For retrograde tracer (Alexa 488-CTB) experiments, fixed brain tissues were sliced into 50-μm-thick sections using a vibratome (5100 mz, Campden Instruments, Lafayette, IN). For other histological experiments, excised brains were equilibrated in 30% sucrose solution in PBS before being frozen and cut into 25-μm-thick sections using a microtome (Leica Microsystems, Wetzlar, Germany). For retrograde tracer (Alexa 488-CTB) experiments, fixed brain tissues were sliced into 50-μm-thick sections using a vibratome (5100 mz, Campden Instruments, Lafayette, IN). After blocking and permeabilization for 1 h in 5% bovine serum albumin (BSA) and 0.5% Triton X-100 in PBS, slices were incubated at 4°C overnight with PBS-diluted primary antibodies. Subsequently, the slices were washed in PBS and incubated with a secondary antibody diluted in PBS at room temperature for 3 h before mounting on glass slides with Fluoromount-G (Southern Biotech, Birmingham, AL, USA). Imaging was performed using a fluorescence microscope (BZ-X700, Keyence, Osaka, Japan), a Zeiss LSM510 Meta confocal microscope (Carl Zeiss) with a 20× objective (NA 1.0; Carl Zeiss) and a 63× oil-immersion objective (NA 1.4), or an Olympus FV3000 confocal microscope (Olympus) with a 10× objective lens (NA 0.3; Olympus). Staining was performed using specific antibodies as mentioned in the table (STAR Methods).

Image analysis after immunostaining

ImageJ (National Institutes of Health) was used for analyzing confocal 3D image data obtained at 20× (1024 × 1024 pixels, 0.313 μm/pixel, 2.0 μm Z-step, 4 slices) or 63× (1024 × 1024 pixels, 0.198 μm/pixel, 0.5 μm Z-step, 31 slices) magnifications. Co-localization was estimated using the ImageJ plug-in and Mander's colocalization coefficient (tM), which ranges from one (complete colocalization) to zero (no colocalization).[82] The fraction of pixels containing signals from both green (IBA1) and red (CD68 or C1Q) fluorescence is given by tM1. VGAT and VGLUT puncta within the microglia were counted on the middle slice of the image stack using the ImageJ Orthogonal view. Neuron-associated microglia were defined as those in contact as follows: (1) firstly we drew a vertical line from the presumed microglial center to the neuronal soma surface; (2) then we measured the signal intensities of microglia-associated green fluorescence (EGFP) and neuron red (Alexa 594; for PV) or blue (Alexa 405; for NeuN) fluorescence along this line using the Multiplot function in ImageJ; (3) we subtracted the standard deviation of the fluorescent intensity of this region of interest (ROI) line from the total fluorescence of the adjacent neuron or microglia (means of signal smoothing), and (4) if there was a gap between the end and the start of the green fluorescence (when the smoothed signal intensity was <2 pixels (0.5 μm)), it was classified as contact between the microglia and neuron. To quantify PV$^+$ terminals around pyramidal neurons, we used the z-projection of slices of the center of the pyramidal neuronal soma (for pyramidal neurons without microglia) or the most adjacent section to microglia (for pyramidal neurons with microglia), dividing the number of PV$^+$ terminals by the neuron perimeter. We used Imaris (Oxford Instruments) to create a 3D reconstructed image (Video S1).

Real-time PCR

Five days after MD, the mice were deeply anesthetized using ketamine (74 mg/kg, *i.p.*) and xylazine (10 mg/kg, *i.p.*) and transcardially perfused with PBS. The brain was excised and the ipsilateral and contralateral V2L cortices were dissected for cell dissociation and microglial separation. Five mice were used for these experiments, and the ipsilateral and contralateral cortices were combined into two samples. Cells were dissociated using a Neural Tissue Dissociation Kit (T) (130-093-231; Miltenyi Biotec, Bergisch Gladbach, Germany). Debris was removed by passing the dissociated brain samples through a cell strainer (40 μm) with 5% BSA-PBS. Subsequently, we used a magnetic-activated cell sorting (MACS) system with CD11b magnetic beads (130-093-634, Miltenyi Biotec) to isolate microglia (CD11b+ cells).[69] Total RNA was extracted using an RNeasy Plus Mini Kit (74134; Qiagen, Hilden, Germany). First-strand complementary DNA (cDNA) was synthesized from total RNA using the Transcriptor First Strand cDNA Synthesis Kit (04896866001; Roche Diagnostics, Mannheim, Germany). Amplification reactions were performed on a LightCycler 96 System (Roche Diagnostics) using FastStart Essential DNA Green Master (06402712001, Roche Diagnostics). Amplification results were analyzed using the LightCycler software and normalized to GAPDH mRNA levels in each sample. The primer sequences have been indicated in the table (STAR Methods).

Immunoblotting

Five days after MD, the mice were deeply anesthetized with ketamine (74 mg/kg, *i.p.*) and xylazine (10 mg/kg, *i.p.*) and transcardially perfused with ice-cold PBS. The brain was excised, and the ipsilateral and contralateral V2L cortices were dissected and separately homogenized in N-PERTM Neuronal Protein Extraction Reagent (87792, Thermo Scientific, Rockford, IL, USA) with a protease inhibitor cocktail (25955, Nacalai Tesque, Japan). After 10 min incubation on ice, homogenates were centrifuged at 10,000 × g (10 min at 4 °C). Concentrations were determined using Pierce™ BCA Protein Assay Kit (23225, Thermo Scientific). After electrophoresis of supernatant by using 4–20% Mini-PROTEAN® TGX™ Gels (4561096, Bio-Rad Lab, Tokyo, Japan), the samples were transferred to Trans-Blot Turbo 0.2-micron PVDF Membrane (SDS) (1704156, Bio-Rad Lab, Tokyo, Japan). The membranes were incubated with anti-beta actin (rabbit, Abcam, ab8227; 1:5,000), anti-VGLUT1 (guinea pig, Synaptic Systems, 135 304; 1:5,000), anti-VGAT

(guinea pig, Synaptic Systems, 131 004; 1:5,000). After exposure to each primary antibody, the membranes were incubated with HRP-conjugated anti-rabbit (donkey, Invitrogen, 31458; 1:50,000) and anti-guinea pig (rabbit, Invitrogen, PA1-28597, 1:50,000) antibodies. Immunoreactive bands were visualized using SuperSignal™ West Pico Plus (34577, Thermo Scientific) for beta-actin and SuperSignal™ West Dura (34076, Thermo Scientific) for VGLUT and VGAT, followed by recording with Fusion Solo S (Vilber Lourmat, France) or iBright™ CL1500 Imaging System (Thermo Scientific, Rockford, IL, USA). Images were analyzed with Fusion-Capt Advance Software version Solo 7 17.00d or iBright™ CL1500 Imaging System.

Sensory training and discrimination tasks

Control, MD, BD, and microglia-ablated mice underwent surgery to attach the head plate, after which they were maintained in their cages on a water-deprived diet throughout the subsequent behavioral experiments. Body weight remained at approximately 82-85% of the preoperative weight. For the behavioral tests, the mice were secured inside a body chamber with their heads fixed between stage-attached holders. Mice were presented with sandpaper during initial training and during the subsequent sensory discrimination task using a water reward. This was adapted from previously described Go/No-go paradigms.[83,84] The mouse's behavior was monitored using an infrared video camera. The timing and control of different devices (water-reward valve, sandpaper presentation, stepper motor, camera), as well as behavioral parameter recordings, used custom-written LabVIEW programs (National Instruments, Austin, TX, USA). Licks were detected from the electrical potential difference between the licking spout (a metal sipper tube wrapped with copper wire) and the body chamber (wrapped with aluminum foil).[85]; Sandpaper was attached to a two-arm wheel mounted on an analog servo and a motorized linear stage (T-LSM100A, Zaber) that moved the appropriate sandpaper within reach of the whiskers. In each trial, either # 80 (rough) or # 400 (smooth; KAKURI Sangyo, Niigata, Japan) sandpaper was moved to the front of the mouse's snout for 3.5 s and then subsequently placed parallel to the rostrocaudal axis of the head for 2 s, with the mouse using its whiskers to investigate the sandpaper. Subsequently, lick responses were recorded. Each trial comprised a 3.0 s baseline, with an auditory cue of a 3-kHz sound for 200 ms, then sandpaper representation of the whisker for 2.0 s, and then lick decision time between 500 ms and 2.0 s after each sandpaper representation (Figure S8A).

The mice initially underwent pre-training that involved only a reward. Specifically, water was rewarded only when mice licked during smooth sandpaper presentation, and this reward was scored as a "hit." The water reward was withdrawn when the rough sandpaper was presented (licking was scored as a miss). Success was scored during the training period as the proportion of hits to misses. Pre-training involved 200 daily trials, and mice with >70% success rates for two consecutive days proceeded to the main discrimination task. For this task, presentation of the smoother #400 sandpaper again was associated with a reward of 7 μL water bolus that was only available when mice licked within the time window (hit). However, when mice licked following the presentation of rougher #80 sandpaper, they received a 500-ms air-puff on the left eye as punishment (false choice) and not licking after rough sandpaper was scored as correct rejection (CR). The discrimination task lasted for four days (200 trials each day), and performance was quantified as a success rate percentage (Hit + CR)/total trials (%). To determine whether the V2L was required for this whisker discrimination task, an Elvax Drug Elution sheet (1 mm × 1 mm) mixed with 100 mM muscimol (Sigma-Aldrich) was applied to the brain surface of the V2L area.[86]

Electrophysiology

Control, MD, and microglia-ablated PV-td-tomato mice (derived from crossing PV-Cre mice and Rosa26-tdTomato reporter mice) were used for electrophysiological experiments at five weeks of age, which was two weeks after the injection of AAV1-Syn-ChR2 (H134R)-EYFP (Addgene; 2.11×10^{13} vector genomes/ml) into the left S1. Mice were deeply anesthetized using isoflurane and transcardially perfused with ice-cold artificial cerebrospinal fluid (ACSF), which contained (in mM) 126 NaCl, 3 KCl, 1.3 $MgSO_4$, 2.4 $CaCl_2$, 1.2 NaH_2PO_4, 26 $NaHCO_3$, and 10 glucose, saturated with 95% O_2 and 5% CO_2. Additionally, 1 mM kynurenic acid was added to reduce neuronal excitotoxicity. Brains were removed and cut as coronal slices (300 μm) containing the visual cortex using a vibrating microslicer (VT1200S; Leica). Slices recovered in an interface chamber at 33 °C for 1 h in a solution of ACSF (without kynurenic acid). Next, the slices were transferred to a submerged chamber containing oxygenated ACSF with 95% O_2 and 5% CO_2 at room temperature (without kynurenic acid). Within the V2L, PV^+ cells were identified by tdTomato fluorescence, and neurons were visualized using infrared differential interference contrast optics at 40X magnification with a water immersion lens (BX-50WI, N.A. 0.8, Olympus). Patch pipettes (5-7 MΩ) were filled with different solutions for recording and stimulating from PV^+ or pyramidal cells. For the PV cells, the pipette solution contained (130 mM) 130 K-gluconate, 8 mM CsCl, 1 $MgCl_2$, 0.6 EGTA, 10 mM HEPES, 3 MgATP, 0.5 Na_2GTP, 10 mM Na-phosphocreatine, and 0.2% biocytin (pH 7.3 adjusted with KOH). For pyr cells, the pipette contained (in mM) 130 Cs-gluconate, 8 KCl, 1 $MgCl_2$, 0.6 EGTA, 10 HEPES, 3 MgATP, 0.5 Na_2GTP, 10 Na-phosphocreatine, and 0.2% biocytin (pH 7.3 adjusted with CsOH). We first obtained whole-cell patch-clamp recordings from PV^+ cells using laser photostimulation, focused through the 40X microscope objective and using 2 ms blue light flashes (440 nm) to determine whether the PV^+ cells received S1 inputs. If there was an S1-evoked response, we subsequently targeted a proximal (<100 μm away) pyramidal neuron for dual whole-cell recordings. The Pyr neuron was on average 45.91 ± 3.409 μm from the PV neuron for control mice, and 50.98 ± 6.697 μm away for MD mice, and 37.18 ± 3.108μm away for ablated MD mice. (Mean ± SEM–; Kruskal-Wallis test, $p = 0.2369$). We recorded from cells with the soma located ≥50 μm below the cut slice surface. To better isolated synaptic connections, we maintained the membrane potential of the recorded cells at the reversal potential of inhibitory (0 mV) or excitatory postsynaptic currents (-70 mV: holding potentials were corrected for the liquid junction potential). For all paired recordings, we assessed the connections between neuron pairs in both

directions by applying depolarizing voltage pulses for 2 ms ($\geq$ 50 trials) to evoke action potentials in one of the cells and recording IPSCs or EPSCs from the other cell. We selected cells using a series resistance <35 MΩ without series resistance compensation (Series resistance for PV cells (Mean $\pm$ SEM): control, 25.10 $\pm$ 0.941; MD, 26.35 $\pm$ 1.098; ablated MD, 25.02 $\pm$ 1.048; Kruskal-Wallis test, p = 0.7252; Series resistance for pyramidal cells: control, 18.03 $\pm$ 1.160; MD, 17.73 $\pm$ 1.032; ablated MD, 16.78 $\pm$ 1.019; Kruskal-Wallis test, p = 0.6669). To measure the paired pulse ratio (PPR) of uIPSCs, double action potentials were induced at 100 ms interval in PV^+ neurons. The paired pulse ratio (PPR) was calculated. Herein, the averaged peak amplitude of first uIPSCs was divided by that of second uIPSCs. The reliability of each transmission of uIPSCs was estimated as the coefficient of variance (CV) of the uISPC amplitude. We recorded the uIPSCs 50 times for each connected cell pair. The CV of the uIPSC amplitude was calculated as follows: the standard deviation of the uIPSCs amplitude divided by the mean value of the uIPSC amplitude. The failure rate of the uIPSCs was calculated by dividing the number of trials with no uIPSC responses by the total number of recorded trials. The latency of photostimulation-evoked EPSCs (in the absence or presence of 1 μM TTX and 100 μM 4-AP) was measured from the light stimulus onset to the EPSC onset. All recordings were performed using a Multiclamp 700 B amplifier, and data were analyzed using the pClamp9 software (Molecular Devices).

Serial block-face SEM

The mice were anesthetized and perfused with PBS, followed by buffering with 4% PFA containing 2.5% glutaraldehyde (pH 7.4). The brains were removed, immersed in the fixative overnight at 4 °C, and cut into 200-μm-thick slices using a vibratome. *En bloc* heavy metal staining was performed, with some modifications.[87] Briefly, the tissues were washed with PBS, treated with 2% OsO_4 in 1.5% $K_4[Fe(CN)_6]$ for 1 h on ice, and filtered through 1% thiocarbohydrazide for 20 min and 2% OsO_4 for 30 min at room temperature. Tissues were then treated with uranyl acetate overnight at 4 °C, and lead aspartate solution at 50 °C for 2 h. Each treatment was followed by five washes with double-distilled water for 10-15 minutes. Tissues were dehydrated in a graded series of ethanol (60, 80, 90%, and 95%, 5 min each) and incubated with acetone, dehydrated using a molecular sieve, a 1:1 mixture of resin and acetone, and 100% resin Durcupan (Sigma). The samples were placed in a mold with conductive resin containing 5% Ketjen black in Durcupan and cured at 60 °C over four nights. The blocks were trimmed and mounted on aluminum rivets using conductive glue (CR-2800; Kaken Tech). After light microscopic identification of layers II and III on semi-thin sections and trimming of the region of interest, the surfaces of the trimmed samples were treated with gold sputtering to increase conductivity and imaged using SBF-SEM, a field-emission scanning electron microscope (Merlin from Carl Zeiss, Germany) equipped with 3View, a system with a built-in ultramicrotome, and a back-scattered electron detector (Gatan, CA, USA). Serial images were processed using ImageJ and Fiji software plugins, and segmentation and image analyses were performed using Amira (FEI). Images were captured at a resolution of 5 nm/pixel in the X- and Y-directions and 40 nm in the Z-direction. Microglia near the neuronal soma were identified using established criteria, which include relatively small and elongated nuclei with clumped chromatin beneath the nuclear envelope, irregular contours of the cytoplasm, and processes with lysosomes and elongated endoplasmic reticulum in serial images.[88,89]

QUANTIFICATION AND STATISTICAL ANALYSIS

All data analyses were performed using the GraphPad Prism 8 and 9 software (GraphPad Software Inc., La Jolla, CA, USA). Data are presented as mean $\pm$ SD, unless otherwise specified. Statistical significance was tested using the unpaired t-test (two-tailed), paired t-test (two-tailed), Mann-Whitney U test (two-tailed), and one-way analysis of variance, followed by Tukey's post-hoc tests, two-way analysis of variance, Tukey's post-hoc tests, chi-squared test, Kruskal-Wallis test, Dunn's multiple comparisons test, and Pearson's correlation test, as specified in the text or Figure legends. A non-parametric Kruskal-Wallis test followed by Dunn's test for more than two groups was applied when the data did not show a normal distribution. Significant differences are indicated in the figures by *p < 0.05, **p < 0.01, ***p < 0.001. Notable non-significant differences are indicated in the figures by N.S. Data S1 includes exact value of n, F-values and degrees of freedom for one-way analysis, and *t*-values and degrees of freedom for t-tests.